ALIGNING CARBON NANOTUBES USING ULTRASOUND TO REINFORCE COMPOSITE MATERIALS

by

Michael Dean Haslam

A thesis submitted to the faculty of
The University of Utah
in partial fulfillment of the requirements for the degree of

Master of Science

Department of Mechanical Engineering

The University of Utah

December 2012

The University of Utah Graduate School

STATEMENT OF THESIS APPROVAL

The thesis of **Michael Dean Haslam**

has been approved by the following supervisory committee members:

Bart Raeymaekers	, Chair	**08/09/2012** Date Approved
Daniel O. Adams	, Member	**08/09/2012** Date Approved
Bruce Gale	, Member	**08/09/2012** Date Approved

and by **Timothy Ameel**, Chair of the Department of **Mechanical Engineering**

and by Charles A. Wight, Dean of The Graduate School.

ABSTRACT

Carbon nanotubes (CNTs) exhibit extraordinary mechanical properties and display a high surface to volume ratio, which makes them a good filler material for polymer based composite materials. Their mechanical properties are most effectively utilized by aligning the tube axis in the direction of the applied loading. Several methods exist to align CNTs, including wet spinning, dry spinning, mechanical stretching, magnetic field alignment, and plasma enhanced chemical vapor deposition. However, the scalability of these methods is limited and, thus, they are only suited to align small amounts of CNTs.

This work introduces a novel technique, based on bulk acoustic waves (BAWs), to align large amounts of CNTs quasi-instantaneously. This technique is employed to fabricate macroscale composite materials with aligned CNTs as filler material. CNTs are first dispersed in the liquid state of a thermoset resin and introduced into a reservoir where the alignment is performed by BAWs. The cross-linking of the resin fixates the aligned CNTs in the resin matrix and produces a composite material with aligned CNTs.

Composite material specimens were produced using this technique with CNT loading rates up to 2 weight percent (wt%). The mechanical properties of these composites were evaluated experimentally and compared against specimens consisting of both randomly oriented CNTs and pure resin matrix material. Composite material specimens with aligned CNTs (0.15 wt %) displayed a 44% and 51% increase in elastic

modulus compared to composite material specimens with randomly oriented CNTs and pure resin material specimens, respectively. However, due to insufficient dispersion of CNTs in the resin matrix a significant increase in elastic modulus and ultimate tensile strength with increasing CNT loading rate was not observed.

Dedicated to my loving parents who encouraged

me to do my best at everything

TABLE OF CONTENTS

ABSTRACT iii

LIST OF FIGURES viii

LIST OF TABLES xi

1 INTRODUCTION 1

1.1 Background and objective 1
1.2 Carbon nanotubes 3
1.3 Short fiber-reinforced composite materials 5
1.4 CNT reinforced composite materials 8

2 ACOUSTIC MANIPULATION 15

2.1 Concept 15
2.2 Modeling 21

3 EXPERIMENTAL APPARATUS 25

4 MANUFACTURING METHOD 31

4.1 Sound speed measurement 31
4.2 Alignment verification 33
4.3 Sample fabrication 33
4.4 Operating domain and limitations 35

5 RESULTS AND DISCUSSION 37

5.1 Degree of alignment 38
5.2 Degree of dispersion 41
5.3 Static testing 49

6 CONCLUSION 58

APPENDIX 61

REFERENCES 67

LIST OF FIGURES

Figure Page

1.1 Computer generated images of a) SWNT and b) MWNT 4

1.2 Computer generated images of a carbon nanotube in a) armchair and b) zigzag configuration with the difference marked in gray 4

1.3 Representation of a single fiber embedded in a matrix 6

1.4 Depictions of a) undeformed shape and b) deformed shape of a single short fiber embedded in a matrix under an applied tension load T. 7

1.5 Length efficiency factor η_l versus length-to-diameter ratio l/d with the minimum value at $l/d = 10$ indicated 9

1.6 SEM micrograph showing bulk entanglement of MWCNTs prior to dispersion 11

1.7 TEM micrograph of the dispersion of CNTs obtained by Pötschke et al. [65] 12

1.8 0.01 wt % water-CNT solution a) before and b) after dispersion by sonication 13

2.1 Acoustic waves, a) progressive wave and b) standing wave with arrows indicating the movement of particles in the wave field 16

2.2 Node and antinode locations of a pressure wave and the corresponding acoustic radiation force (see Eqs. (2.3) and (2.4)) 18

2.3 Direction of the applied acoustic radiation on a circular cylinder for all theoretical derivations 19

2.4 Acoustic radiation force on a cylinder whose center is located on a node 20

2.5 A schematic showing a) the polarity of a PZT plate and the applied electrical charge that produces b) expansion and c) contraction 21

2.6 PZT polarity setup at a fixed separation to establish an a) even number of nodes and b) odd number of nodes 22

2.7 Comparison of experimental to theoretical distance between nodes of the standing pressure wave using a) SEM b) optical microscope 24

3.1 Experimental apparatus 25

3.2 Top view of the reservoir with dimensions in millimeter 27

3.3 Direction of the expansion/contraction of the PZT for determining k_t and d_{33} 27

3.4 SEM image of the CNTs purchased from CheapTubes.com 29

4.1 Setup to measure the sound speed in viscous media 32

4.2 Observed alignment of CNTs in the liquid resin using a 1.477 MHz frequency at amplitude of 250 mVpp with the distance between lines indicated 33

4.3 Schematic of the extraction technique to evacuate the composite material specimen from the mold using a die punch 34

4.4 Composite material specimen with aligned CNTs (1 wt% loading rate) showing aligned CNTs in the gauge length of the dog-bone sample 35

5.1 Hermans' orientation factor H versus average angle between the fiber axis and the composite alignment axis ϕ 39

5.2 Microscale alignment, a) unprocessed image and b) processed image showing black CNT clusters overlaid with gray lines along their axis for determining the Hermans' orientation factor of a specimen 40

5.3 Processed SEM images at a) 500 nm and b) 50 μm magnification levels to calculate a Hermans' orientation factor 41

5.4 Comparison of the dispersion index calculation for a) the ASTM standard and b) the index developed in this work 43

5.5 Benchmark images used to compare the ASTM index to the new index. a) shows a random computer generated 5 vol% sample, b) and c) show two variations of a 5 vol% sample 46

5.6 Sample images to compare the ASTM index to the new index at 3 different vol% loading rates; a) 2.9% b) 5.6% c) 10.7% vol%, corresponding to 0.5, 1, and 2 wt%, respectively 46

5.7 Dispersion versus CNT loading rate in wt%.....49

5.8 Mechanical testing, a) Dog-bone sample installed in the load frame, b) a close up image of the clamped specimen.....50

5.9 Nondimensional elastic modulus results with 90% confidence intervals versus CNT loading rate [wt%] 52

5.10 Nondimensional ultimate tensile strength results with 90% confidence intervals versus CNT loading rate [wt%].....52

5.11 Nondimensional ultimate tensile strength version dispersion for all composite material samples. A linear fit and 90% confidence interval are also included 56

5.12 Selected fracture surface images processed for dispersion quantification, a) 0.15 wt% with randomly oriented CNTs, b) 1.00 wt% with randomly oriented CNTs, c) 0.50 wt% with randomly oriented CNTs, and d) 1.00 wt% with aligned CNTs.....56

LIST OF TABLES

Table		Page
2.1	Comparison of the predicted frequencies to the observed frequencies that create alignment of CNTs	23
3.1	Properties of the PZT plates used in the apparatus [104]	27
3.2	Properties of the Smooth-Cast 300 resin [105]	29
3.3	Properties of the MWNTs [106]	29
4.1	Sound speed measurement results for different viscous media	32
4.2	Range of parameters used for the manufacturing method	35
5.1	Types and quantities of CNT composite material specimens analyzed in this work	38
5.2	Hermans' orientation factor results obtained for five samples	40
5.3	Dispersion index results from the ASTM index and the compIndex (dIndex and sIndex) for six test images	46
5.4	Average dispersion index results for all composite material samples made in this work	48
5.5	Summary of static testing results displayed in Figs. 5.9 and 5.10	53
5.6	Comparison of theoretical and experimental results for the elastic modulus	54

CHAPTER 1

INTRODUCTION

1.1 Background and objective

Carbon nanotubes (CNTs) have been studied extensively since their discovery in 1991 [1]. They exhibit extraordinary mechanical, thermal, and electrical properties, and can be used in a wide range of applications such as batteries, sensors, nanoscale probes, electronics, hydrogen storage, and composites [2]. The addition of CNTs into polymer composites can greatly enhance their mechanical properties [3]. However, to take full advantage, their tube axis needs to be aligned with the direction of the applied load [4].

Many researchers have investigated integrating CNTs into a polymer matrix to improve the mechanical [5], electrical [6], or thermal [7] properties of the resin. Here we focus on the improved mechanical properties afforded by the addition of CNTs to the polymer matrix. Recent studies, for example, demonstrated an increase in the elastic modulus E from 1.2 GPa to 2.4 GPa upon the addition of 1 weight percent (wt%) CNTs [8] and from 4.2 GPa to 5.0 GPa upon adding only 0.1 wt% CNTs [9]. Even though loading rates up to 60 wt% [10] have been accomplished in spun fibers, typical loading rates in bulk composites are much lower, ranging between 0.01 – 10 wt% [11]. The tensile strength of these composite materials does not increase with the loading rate as predicted by composite material models [12], one notable exception observed an increase

in tensile strength up to a loading rate of 20 wt% [13]. This was accomplished by grafting matrix material into the CNTs during their synthesis. It is this grafting that gives the final composite a greater strength even at high loading rates. No other publication could be found to successfully employ this technique, however.

In forming CNT composite materials, two factors have been of interest: dispersion [14-21] and alignment [22-26] of the CNTs in the polymer matrix. These two factors are the most critical problems that need to be overcome to effectively employ CNTs as high-strength filler materials in composite materials [3, 11, 27-29]. Dispersion is difficult to obtain because CNTs tend to bundle together by large van der Waals forces [6]. However, to achieve load transfer between the polymer matrix and the CNT filler, a bond between both constituents is imperative [30]. Functionalization of the CNTs by chemical preprocessing has recently been demonstrated to significantly enhance their processibility [31] and increase the load transfer from the matrix to the CNT filler [32]. This promises to relieve some of the problems related to dispersing CNTs into a matrix. While several alignment methods have been demonstrated in the literature [33-38] (see appendix), they are mainly limited by their scalability, and only suited to align small amounts of CNTs.

In this thesis, a new scalable technique to align CNTs based on bulk acoustic waves (BAWs) is developed. BAWs have previously been used to manipulate microscale particles [39-41], cells [42-44], and nanoparticles [45]. Here, CNTs are dispersed in the liquid state of a thermoset resin and subsequently aligned into parallel rows using BAWs. The obtained pattern is fixated by the cross-linking of the resin, which yields a polymer composite material with aligned CNTs.

The objective of this work is to

(1) test the hypothesis that CNTs can be aligned using bulk acoustic waves in a macroscale volume of polymer matrix material,

(2) quantify the degree of alignment obtained with this method, and

(3) use this novel technique to fabricate macroscale composite materials with aligned CNTs and measure their mechanical properties under static loading. The mechanical properties of these composites will be compared against composite material specimens consisting of both randomly oriented CNTs and pure resin material. Different CNT loading rates will be considered.

1.2 Carbon nanotubes

CNTs are cylindrical carbon nanostructures made from a monolayer graphite sheet rolled into a tube. Two varieties of CNTs exist; single-walled nanotubes (SWNTs), which consist of a single carbon wall, and multiwalled nanotubes (MWNTs), which contain several concentric tubes inside each other [2], as shown in Figs. 1.1a) and 1.1b), respectively. SWNTs and MWNTs can be further classified by their chirality, defined as the angle at which the graphite sheet links together to form a tube. Nanotubes with armchair and zigzag chirality are shown in Fig. 1.2 and represent a graphite sheet that has been rolled up in each of the two orthogonal directions. Chiral nanotubes are a variation of the two former types and encompass all angles that are not orthogonal. CNTs have been fabricated with length-to-diameter ratios up to 136,000,000:1 [46] and diameters ranging between 0.4 nm - 100 nm [2]. The three most common methods to fabricate CNTs are arc discharge, laser ablation, and chemical vapor deposition (CVD) [47].

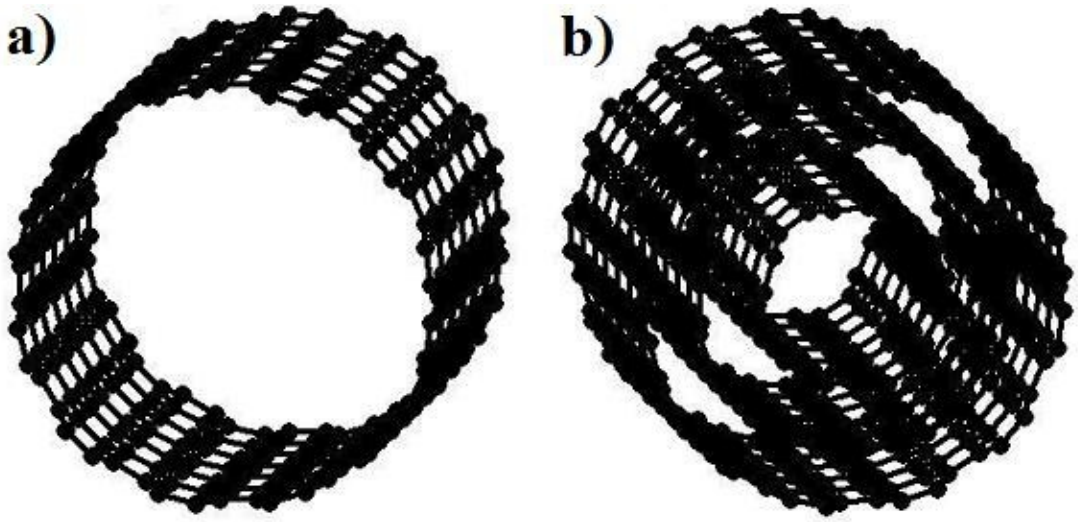

Figure 1.1: Computer generated images of a) SWNT and b) MWNT

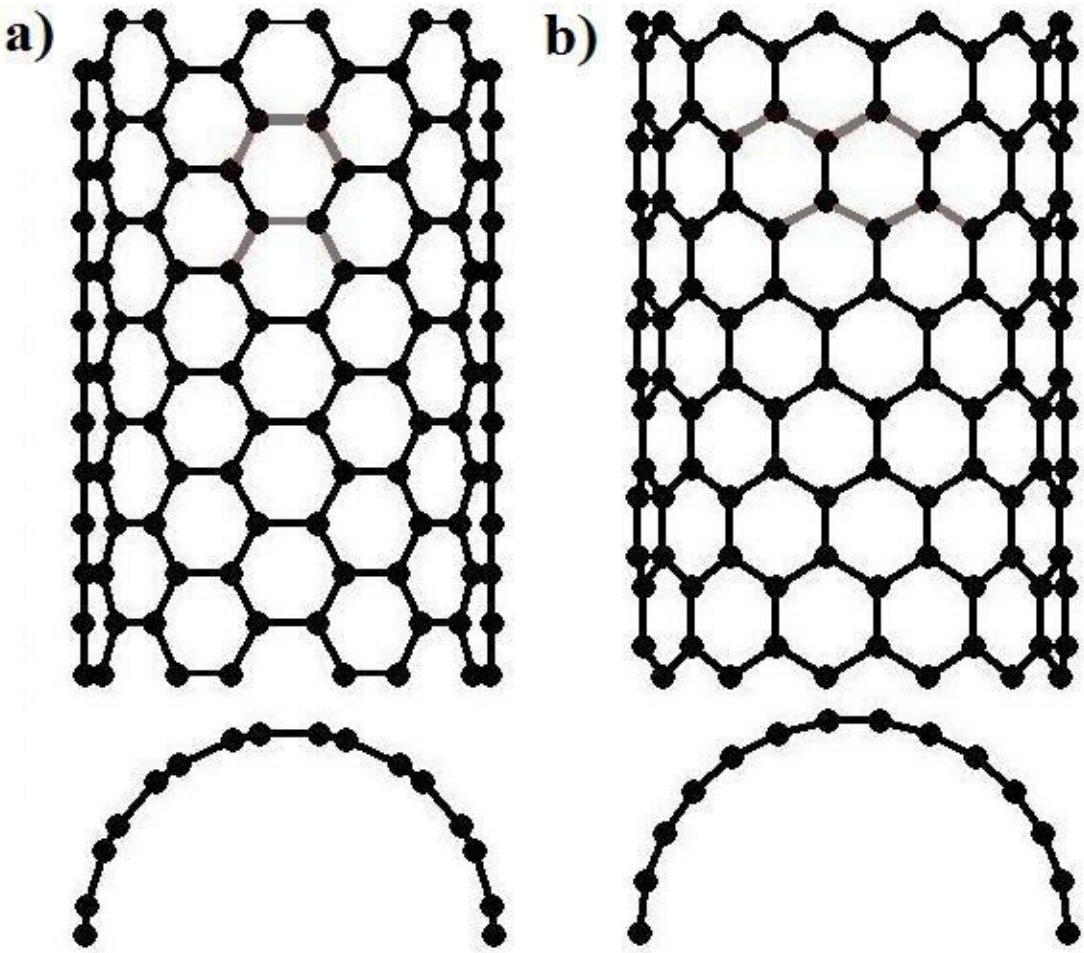

Figure 1.2: Computer generated images of a carbon nanotube in a) armchair and b) zigzag configuration with the difference marked in gray

The properties of CNTs are extraordinary. It has been shown that they are stronger than steel, lighter than aluminum, and more conductive than copper [47]. The elastic modulus in the direction of the tube axis is approximately 1 TPa [48]. The ultimate tensile strength in this direction is 150-180 GPa [49]. Hence, nanotubes have an elastic modulus five times larger than steel and a tensile strength 200 times larger than medium strength carbon steel. These mechanical properties combined with a low density of approximately 1.87 g/cm^3 [50] yields an extremely high strength-to-weight ratio and render them a good filler for composite materials [28].

1.3 Short fiber-reinforced composite materials

To better understand the use of CNTs in composite materials, a basic knowledge of the mechanics of short fiber-reinforcement is required. There are three primary types of short fiber composite materials: aligned fibers, off-axis aligned fibers, and randomly oriented fibers. While several models for all three types exist, the simplest and most pertinent to this work, aligned fibers, will be discussed here.

A force balance in the axial direction is applied to a single fiber embedded in a matrix as shown in Fig. 1.3, which results in Eq. (1.1) when the normal stress at the ends of the fiber is considered negligible. In this equation σ_f is the normal stress acting on the fiber as a function of the position along the fiber x, τ is the interfacial shear stress as a function of the position along the fiber, and d is the diameter of the fiber. The interfacial shear stress must be known to solve this equation. Two primary models exist: the Kelly-Tyson model in which the matrix is considered a rigid plastic and the Cox model in which the matrix is considered a linear elastic material. In either case the load transfer

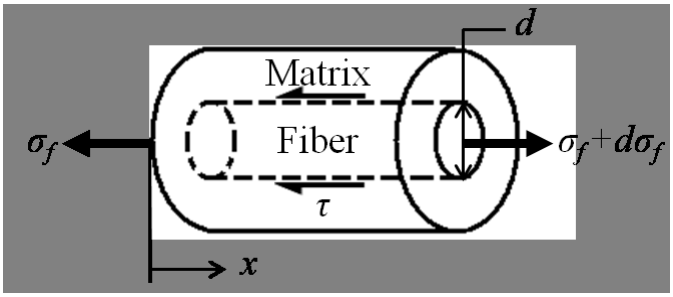

Figure 1.3: Representation of a single fiber embedded in a matrix

$$\frac{d\sigma_f}{dx} = \frac{4\tau}{d} \tag{1.1}$$

from the matrix to the fiber occurs only at the ends of the fiber where the interfacial shear stress is the largest [12]. Figure 1.4 depicts the undeformed (Fig. 1.4a)) and deformed shape (Fig 1.4b)) of a short fiber embedded in a matrix that has been tensioned with a load *T* in the axial direction.

The elastic modulus for this composite material has been determined by several models such as the Kelly-Tyson, Cox, Gibson, and Halpin-Tsai [12]; but only the Cox model will be discussed because it has an alignment factor added by Krenchel [51] that will be used in the analysis of the composites produced in this work (see Chapter 5). Cox assumed that the interfacial shear stress is proportional to the difference between the displacements of the fiber *u* to that of the matrix if no fiber was present *v*. Substituting this assumption into Eq. (1.1) yields Eq. (1.2), where *P* is the axial load as a function of the position along the fiber and *H* is a proportionality constant. This equation is the basis for determining the elastic modulus of the composite. First the normal stress in the fiber is determined by a combination of the homogenous and particular solutions to Eq. (1.2) taking into account appropriate boundary conditions. Equation (1.3) can be derived using

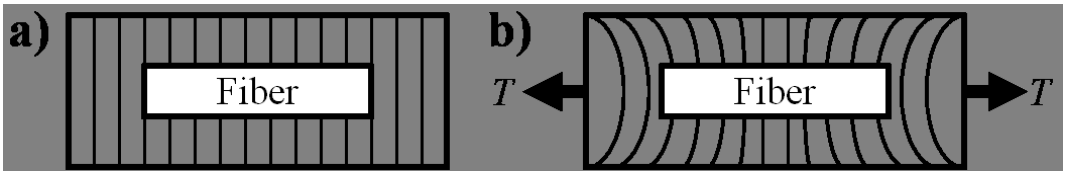

Figure 1.4: Depictions of a) undeformed shape and b) deformed shape of a single short fiber embedded in a matrix under an applied tension load T.

the solution from Eq. (1.2), the rule of mixtures, Hooke's law, and a uniform strain assumption. Equation (1.3) is the solution of the Cox model [52], which describes the elastic modulus of the composite material E_c as a function a length efficiency factor η_l (see section 1.4), the elastic modulus of the matrix material E_m, the elastic modulus of the fiber material E_f, and the volume fraction of the fiber V_f.

$$\frac{dP}{dx} = H\left(u - v\right) \tag{1.2}$$

$$E_c = \left(\eta_l E_f - E_m\right)V_f + E_m \tag{1.3}$$

This result, while useful, is developed without considering the matrix material at the ends of the fiber. Thus, its predicted modulus is closer to that of a continuous fiber composite. Hwang and Gibson developed a modified Cox model that takes into account the matrix material at the ends of the fiber. This is accomplished by weighing the elastic modulus of the Cox model by the volume fractions of the amount of material that applies to the Cox model V_c and the amount of pure matrix material V_m. The elastic modulus E_{mc} is shown in Eq. (1.4) and has been shown to more closely correlate to finite-element

modeling results [53].

$$\frac{1}{E_{mc}} = \frac{V_c}{E_c} + \frac{V_m}{E_m} \tag{1.4}$$

Short fiber composite materials can yield a substantial increase in the elastic modulus if the interfacial shear stress between the matrix and the fiber is sufficient to transfer the load. They also have advantage over continuous fiber composites when complex shapes must be manufactured. These shapes can be injection molded with a short fiber-reinforced material, something that cannot be accomplished with continuous fibers. These composites are also less expensive to manufacture, which all combines, in some cases, to make them the ideal material.

1.4 CNT reinforced composite materials

Coleman et al. [11] state that a filler material must meet four requirements to provide effective reinforcement of a polymer matrix: 1) high length-to-diameter ratio *l/d*, 2) high dispersion, 3) high degree of alignment, and 4) high interfacial shear stress transfer. Each aspect will be discussed to show the suitability of CNTs as filler material.

While a length-to-diameter ratio as high as 136,000,000:1 has been obtained [46], commercially produced nanotubes typically have a length-to-diameter ratio in the range of 100:1-1000:1 [54]. The CNTs used in this work have a length-to-diameter ratio of approximately 250:1 (see Chapter 3). The need for a high length-to-diameter ratio can be seen in the Cox model of Eqn. (1.3). In this equation there is a length efficiency factor η_l

that is a function of the length-to-diameter ratio. Cox found that $\eta_l > 0.90$ is required for effective filler material. The length efficiency factor is plotted in Fig. 1.5 and indicates that an l/d >10 is needed to yield $\eta_l > 0.90$. The length-to-diameter ratio of typical CNTs, as well as the ones used in the present work, exceeds the minimum length-to-diameter ratio by at least one order of magnitude.

Dispersion of CNTs in the polymer matrix is essential to form a bond between the CNTs and the polymer matrix. This is critical to transfer the load from the matrix to the filler reinforcement material. Coleman et al. [11] concluded that this is the most critical problem for CNT reinforced composites and Moniruzzaman et al. [47] found that CNTs are often insoluble in polymers further inhibiting their dispersion. Ajayan et al. [27] demonstrated this problem by measuring the stress transfer from the matrix to the CNTs. They ultrasonically dispersed 5 wt% CNTs in an epoxy resin and allowed it to cure.

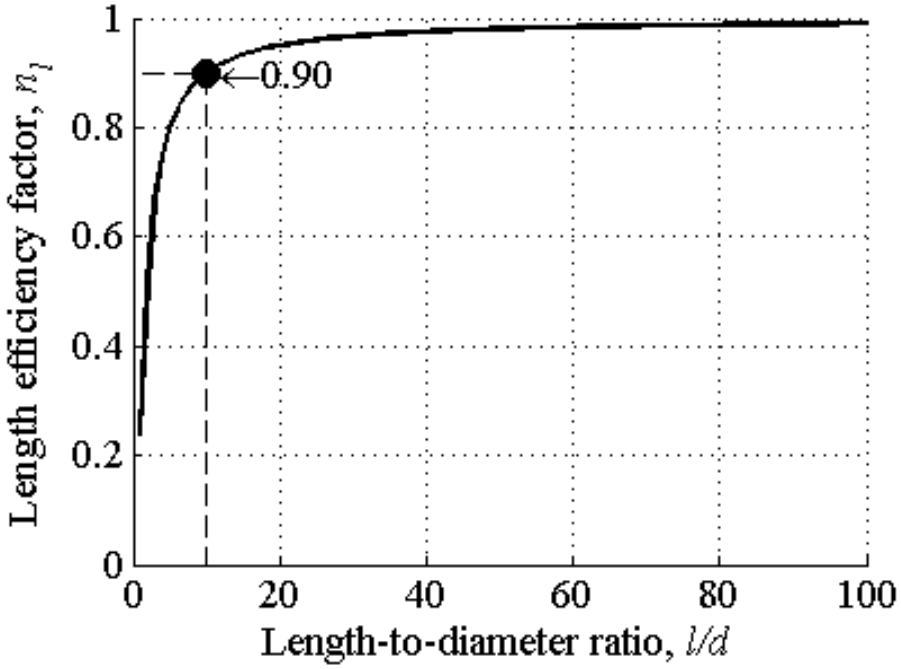

Figure 1.5: Length efficiency factor η_l versus length-to-diameter ratio l/d with the minimum value at l/d = 10 indicated

These samples were then loaded in compression and tension while micro-Raman spectroscopy was used to quantify the stress transfer between the matrix and the CNT filler material. This technique is often used to study the strength of nanocomposites because the strain can be measured by a peak shift in the response [55, 56]. Ajayan et al. showed that as an aggregate of CNTs increases in size, the elastic and shear moduli decrease dramatically. They concluded that individual CNTs are sliding within a bundle of CNTs because they are not bonded to the matrix material. Their work emphasizes the necessity of dispersing the CNTs in the matrix material to successfully utilize their strength.

Girifalco et al. [57] numerically calculated the van der Waals attraction force that holds two identical neighboring SWNTs together using a Leonard-Jones potential for carbon to carbon atoms. Sun et al. [58] continued the work by Girifalco for two SWNTs of different radius. Sun found significantly lower cohesive energy values, but on the same order of magnitude as those found by Girifalco. Although their findings indicate a low attraction force per Å, high bonding energies can exist between individual CNTs due to their extremely long length (approximately 100,000 Å). Girifalco et al. concluded that due to this high bonding energy CNTs will orient themselves parallel to each other "whenever possible." However, this self-alignment does not occur often because CNTs are typically purchased and produced in bundles [59]. The CNTs in these bundles accumulate into large aggregates of overlapping and entangled nanotubes, which is another reason why dispersion of CNTs is difficult to achieve [60]. Figure 1.6 depicts a scanning electron microscope (SEM) micrograph of this entanglement of CNTs obtained by depositing a solution of water and < 0.01 wt % concentration of CNTs on a glass slide

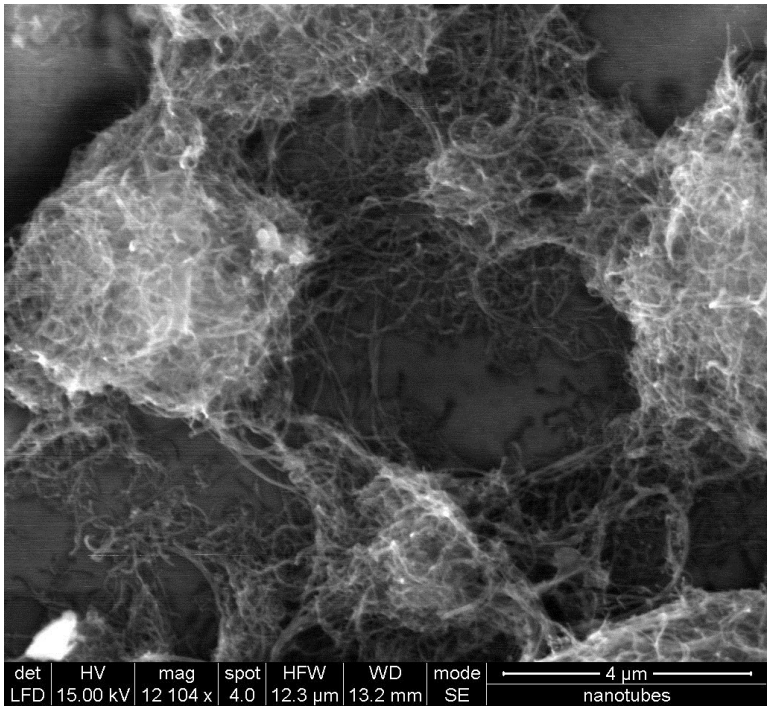

Figure 1.6: SEM micrograph showing bulk entanglement of MWCNTs prior to dispersion

and allowing the water to evaporate. The CNTs in the image are MWNTs that have a diameter ranging between 50-80 nm and a length between 10-20 µm.

Several techniques have been utilized to overcome the van der Waals forces holding the CNTs together including sonication [17, 21, 61], high speed stirring [19], the addition of a compatibilizer or surfactant [16, 18, 62], and melt or shear mixing [63-65]. Often a combination of these methods is employed to further enhance dispersion [60].

Pötschke et al. [65] created CNT polycarbonate (PC) composite materials using a melt mixing and extrusion technique. Plain PC and a 15 wt % mixture of CNT-PC composite was added to a melt mixer in amounts needed to obtain the desired wt% batch. This compound was mixed for 5 minutes and then extruded as a strand of 2 mm in diameter. Samples were then cut both perpendicular and parallel to the strand and analyzed using transmission electron microscopy (TEM) and atomic force microscopy

(AFM). Figure 1.7 shows a TEM micrograph of a 5 wt% CNT-PC composite sample created by Pötschke et al. They determined that all of their samples had a perfect dispersion index of 100 according to the method described in ASTM D2663. The ASTM dispersion index will be discussed in detail in Chapter 5, but it is not the only method used in the literature to quantify dispersion. Others include a statistical relative dispersion index [14] and a UV-visible spectroscopy technique [61]. The former is applied to microscopy images and the latter is used in aqueous solutions of CNTs. Individual CNTs are active in the UV-visible spectrum but large aggregates are not. As an illustration, a 0.01 wt % water-CNT solution was composed and dispersion was achieved through bath sonication for 8 minutes at a power of 35 Watts. Photos of the solution before and after sonication are displayed in Fig. 1.6. Since a UV-visible spectrometer was not available, it was only possible to qualitatively observe the large increase in absorbance before (Fig. 1.8 a)) and after (Fig. 1.8 b)) sonication. This qualitative result indicates that the method

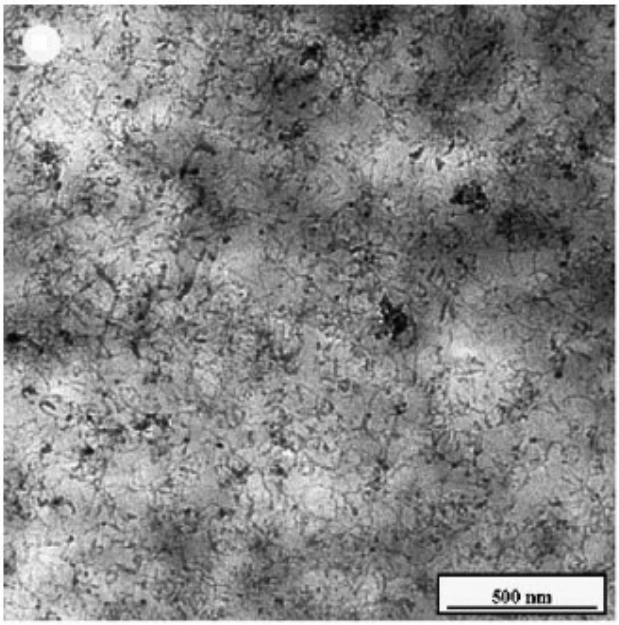

Figure 1.7: TEM micrograph of the dispersion of CNTs obtained by Pötschke et al. [65]

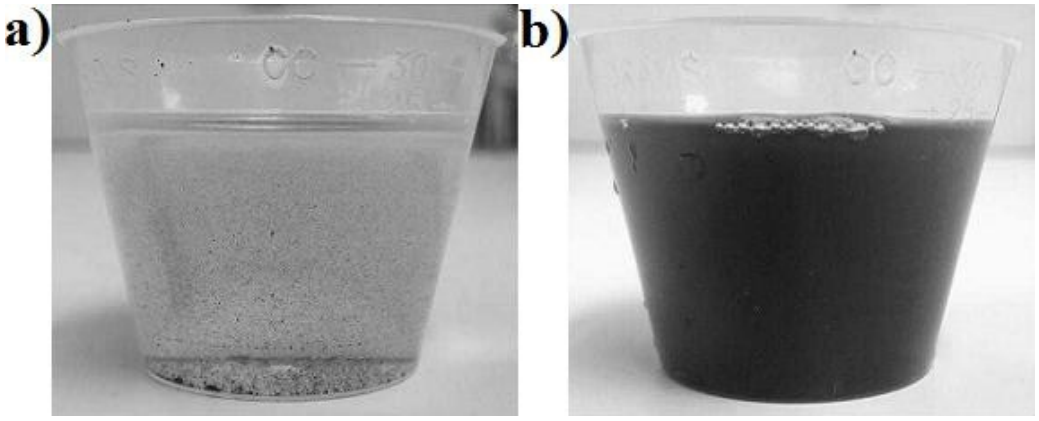

Figure 1.8: 0.01 wt % water-CNT solution a) before and b) after dispersion by sonication

can be effective for determining the dispersion of CNTs in aqueous solutions. While the quantification methods for dispersion vary, it has been shown that good dispersion of CNTs can be achieved.

Filler material must also display a high interfacial shear stress to transfer loading from the matrix to the filler material. This is evident from the Cox model described in section 1.3. Schadler et al. [30] discussed three mechanisms in which this is accomplished: 1) micromechanical interlocking between the fiber and the matrix, 2) van der Waals forces, and 3) chemical bonding. The mechanical interlocking is not likely to occur because CNTs have an atomically smooth surface [7]. Although an attractive van der Waals force has been demonstrated [66], this force is not large enough to transfer a significant load. Chemical bonding of the CNT filler to the matrix is required for substantial load transfer. This has been improved by chemical functionalization of the CNTs [31]. The strength of this bond was partially measured by Wagner et al. [67] and was found to be on the order of 500 MPa. Wagner et al. state that this is comparable to the strongest known filler material and demonstrates that CNTs are excellent candidates to be used as filler material.

The final requirement for a good filler material is high alignment. Several techniques have been documented in the literature to align CNTs in composite materials or in composite fibers. These include wet spinning [37, 68], melt spinning [38, 69, 70], direct spinning [36], the use of liquid-crystal [24] or high strength magnetic fields [25, 35, 71, 72], and mechanical stretching [34]. Slicing composites has also shown to perform alignment in the cutting plane [22, 73] and CNTs can be grown in an aligned manner using plasma enhanced CVD [33, 74]. These methods are discussed in detail in the appendix to provide a complete comparison to the method of ultrasound manipulation developed and presented in this work.

CHAPTER 2

ACOUSTIC MANIPULATION

2.1 Concept

Acoustic manipulation involves the use of a pressure wave in a liquid host medium to manipulate and orient particles or structures in a user-defined pattern. When an acoustic pressure wave propagates through a fluid, a flow of energy is produced [75]. The energy density experienced by an object subject to the pressure wave varies across its surface. This results in a net force that can be used to manipulate the object and is known as the acoustic radiation force. The acoustic radiation force acting on spheres [76-82] as well as cylinders [83-88], has been documented in the literature.

Two types of sound waves are discussed in the literature to manipulate particles; progressive waves and standing waves, both illustrated in Fig. 2.1. A progressive sound wave is created by a single acoustic source, which produces an acoustic radiation force that moves the object in the direction of the propagating wave as indicated in Fig. 2.1a). A standing wave is established by two opposing, parallel acoustic sources, or a single acoustic source with an opposing reflector. The two resulting waves are superimposed to establish a standing wave, and create locations where the net acoustic radiation force is zero. These locations coincide with the nodes or antinodes of the standing pressure wave, and are determined based on the material properties of the particles and the host fluid.

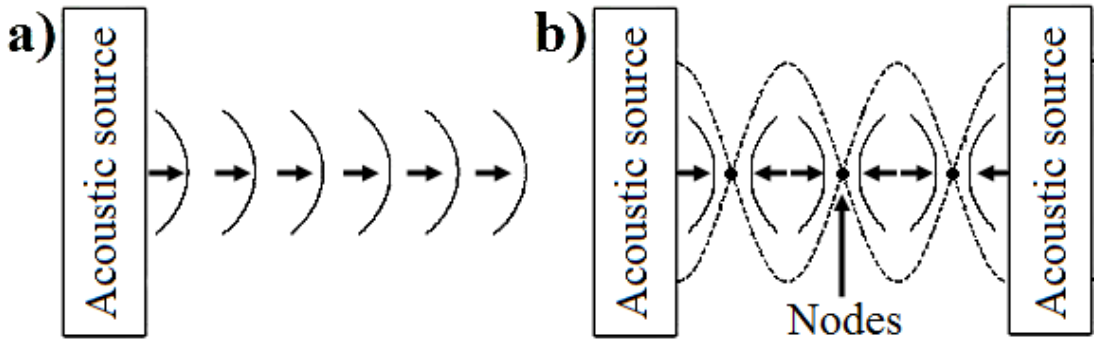

Figure 2.1: Acoustic waves, a) progressive wave and b) standing wave with arrows indicating the movement of particles in the wave field

The acoustic contrast factor Φ determines whether particles subject to acoustic radiation force accumulate at the nodes (Φ > 0) or antinodes (Φ < 0) of the standing pressure wave, and is given as

$$\Phi = \frac{5\rho_p - 2\rho_m}{2\rho_p + \rho_m} - \frac{\beta_p}{\beta_m} \tag{2.1}$$

where, ρ and β represent the density and compressibility of the particle, respectively. Their subscripts indicate whether they apply to the particle p or the medium m. Fig. 2.1b) illustrates the case of CNTs in a solvent or polymer matrix, for which Φ > 0. The movement of the CNTs is indicated by horizontal arrows. Hence, by controlling the locations of the nodes or antinodes of a standing pressure wave, the locations where objects subject to the acoustic radiation force will accumulate can be controlled. This has been demonstrated previously by theoretical modeling [39], and by experimental work [75]. In this thesis, the nodal positions of a standing wave field established by the use of two acoustic sources will be used to manipulate and align CNTs in a polymer matrix.

The frequency f at which a standing wave can be established is given as

$$f = \frac{c}{\lambda} = \frac{cn}{2d} \tag{2.2}$$

where c is the sound speed in the (matrix) medium, λ is the wavelength, n is the number of nodes, and d is the distance between the two acoustic sources, or between the acoustic source and the reflector. This equation shows that the distance between acoustic sources must be a multiple of half the wavelength, as demonstrated previously [75].

The pressure P at any location in a standing wave field can be obtained from [87],

$$P = P_a \cos(\omega t - kx) + P_a \cos(\omega t + kx) \tag{2.3}$$

where P_a is the pressure amplitude, ω is the angular frequency, k is the wave number (defined as $2\pi f/c$), t is the time, and x is the distance from the acoustic source. The equation that describes the acoustic radiation force F resulting from a pressure wave is rather complex. However, it can be shown to be of the following form [86-88]

$$\frac{F}{L} = F_a \sin(2kx) \tag{2.4}$$

where L is the length of the cylinder and F_a is the amplitude of the force. This simple form is obtained by lumping constant factors into F_a, making it a function of the wave amplitude, the scattering coefficients of the wave, the density of the medium, c, k, and the

radius of the cylinder.

Equations (2.3) and (2.4) are used to produce Fig. 2.2, which is a general example that indicates the normalized acoustic radiation force and the normalized pressure magnitude versus the nondimensional distance from the pressure source. The location of the nodes/antinodes of the pressure wave is also indicated. Particles move along the positive x-direction when the acoustic radiation force is positive and along the negative x-direction when the acoustic radiation force is negative, as indicated by the horizontal arrows. The areas where particles accumulate are marked in Fig. 2.2 and are observed to coincide with the nodes of the pressure wave.

The theoretical work performed for spheres and cylinders applies only to structures whose radius is much smaller than the wavelength of the sound wave. This assumption is valid for the manipulation of CNTs as their typical diameter is < 100 nm,

.

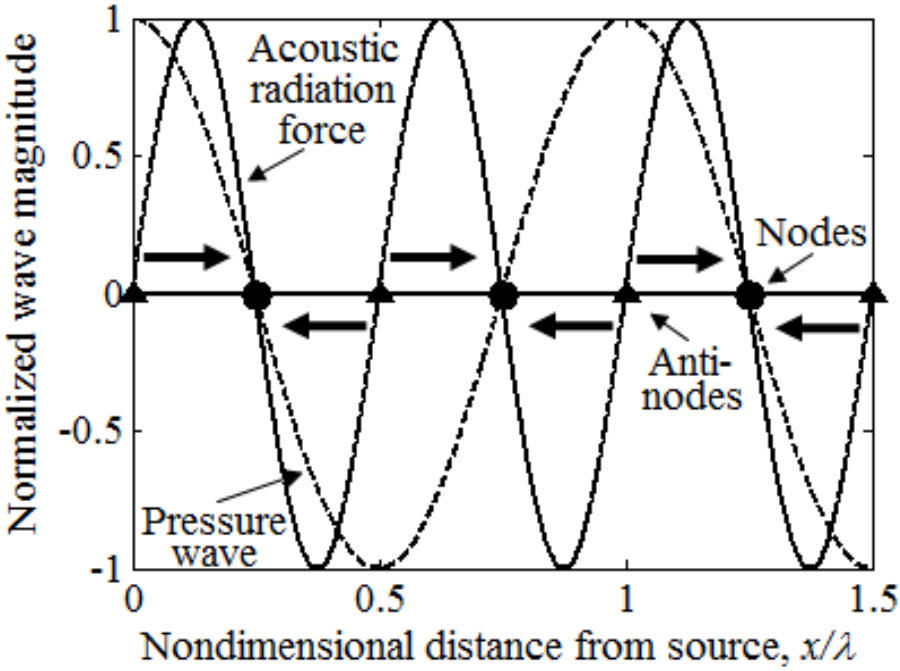

Figure 2.2: Node and antinode locations of a pressure wave and the corresponding acoustic radiation force (see Eqs. (2.3) and (2.4))

which is several orders of magnitude smaller than the wavelength of the ultrasound frequencies used in this work. Another common assumption in the literature is to consider an infinitely long cylinder with the axis of the cylinder perpendicular to the direction of the acoustic radiation force, as depicted in Fig. 2.3. The literature does not provide information on the effect of the acoustic radiation force on a cylinder that is not oriented in this ideal position. We hypothesize that when one part of the cylinder reaches a node and experiences zero force, the remainder of the cylinder continues to feel a net force driving it toward the node, ultimately reaching alignment. A two-dimensional (2D) depiction is shown in Fig. 2.4. In 3D the node would be a plane rather than a line and the cylinder would be free to rotate within that plane. Therefore, manipulation of particles using BAWs in this manner performs an in-plane alignment of particles.

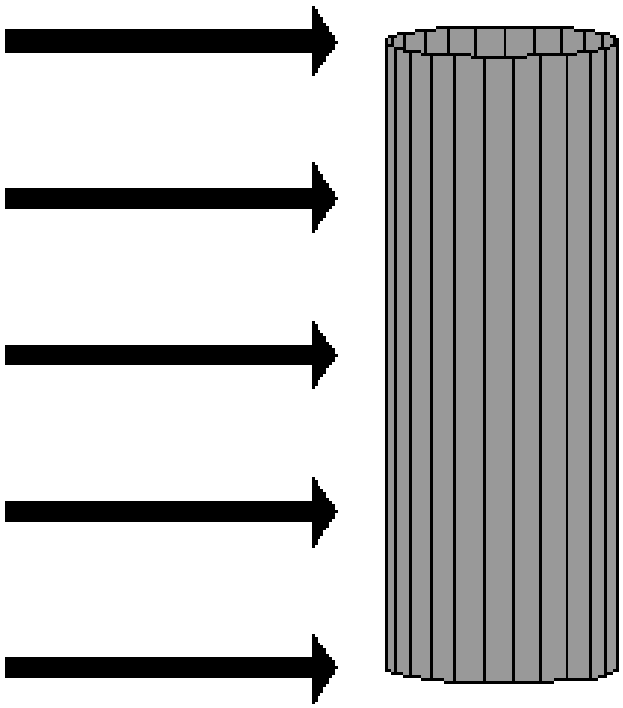

Figure 2.3: Direction of the applied acoustic radiation on a circular cylinder for all theoretical derivations

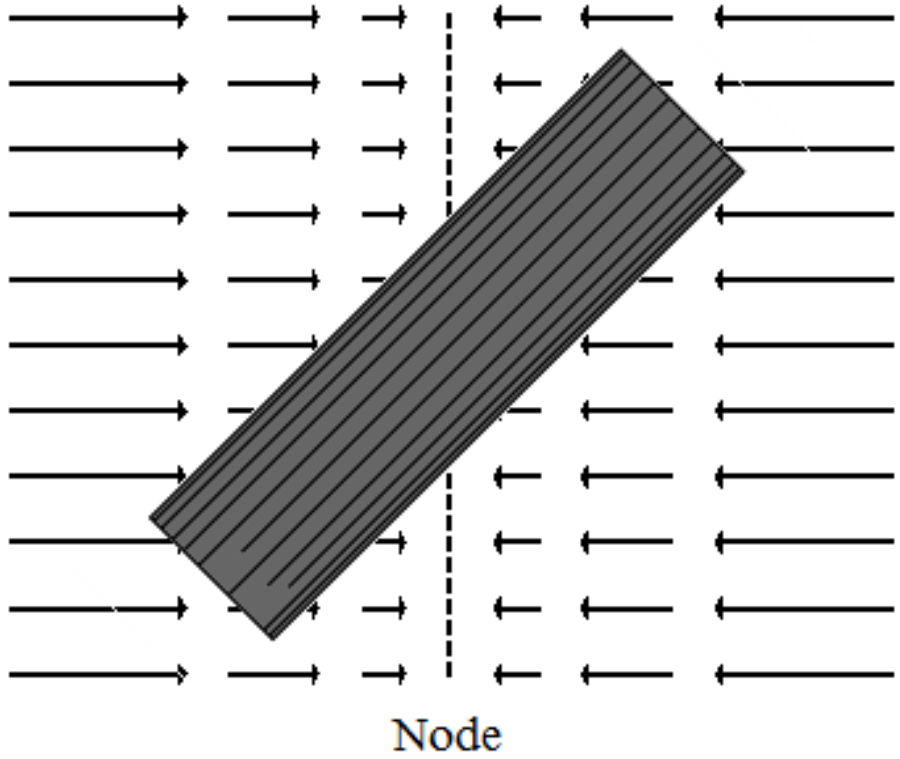

Figure 2.4: Acoustic radiation force on a cylinder whose center is located on a node

The movement of particles by BAWs can occur only when the acoustic radiation force exceeds the drag force acting on the particle. The drag of spheres and cylinders in a viscous fluid is a problem that has been covered extensively in the literature [89-93]. In theoretical analysis at low Reynolds numbers, classical Stokes drag is often used to predict the drag force acting on a particle moving through a fluid. The acoustic radiation force can be increased to overcome the drag force by increasing the amplitude of the pressure wave. However, when the amplitude is increased too far, acoustic streaming, a constant circulatory flow that can result in oscillating fluids [94], may disrupt the formation of nodes. By carefully tweaking the amplitude of the pressure wave, a net force can be produced that drives the nanoscale structures into alignment at the nodes of the pressure wave.

2.2 Modeling

Equation (2.2) is used to determine the resonant frequencies f for which a standing wave is established in a reservoir with distance d between acoustic sources and filled with a medium of sound speed c. Since c (at constant temperature) and d are constant, f is determined by the desired number of nodes n.

In this work two parallel lead zirconate titanate (PZT) plates are used as the acoustic sources for producing a standing wave. Piezoelectric plates have a polarity that dictates whether the applied electric charge will cause expansion or contraction of the plate, as shown in Fig. 2.5. The expansion and contraction of the plates must work in perfect harmony to produce a standing wave. This can be achieved in one of two ways: the two plates can expand and contract simultaneously or one plate can expand while the other contracts. The former can only produce a standing pressure wave with a multiple of full wavelengths, creating an even number of nodes. The latter can only generate a standing pressure wave with an odd multiple of half wavelengths, which creates an odd number of nodes. Thus the polarity must be considered to properly predict the resonant frequencies of a two PZT plate setup from Eq. (2.2).

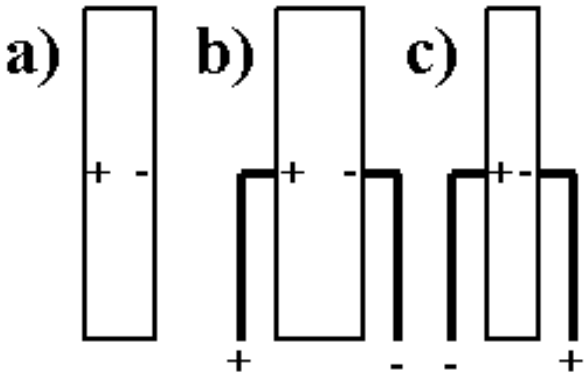

Figure 2.5: A schematic showing a) the polarity of a PZT plate and the applied electrical charge that produces b) expansion and c) contraction

The setup for producing an even number of nodes and an odd number of nodes by the use of two parallel PZT plates a fixed distance apart is illustrated in Fig. 2.6. To produce an even number of nodes the polarity of the PZT plates is set to expand and contract simultaneously and the frequency is set to the value obtained from Eq. (2.2) for an even number; this setup is shown in Fig. 2.6a) for $n = 4$. To produce an odd number of nodes, the polarity of one plate is reversed and the frequency is adjusted to the value from Eq. (2.2) for an odd number; this setup is shown in Fig. 2.6b) for $n = 3$.

Using a reservoir filled with water ($c = 1495$ m/s) with two opposing, parallel PZT plates separated by $d = 14.08$ mm, the theoretical frequencies (Eq. 2.2) to create an odd number of nodes ($15 \leq n \leq 27$) are compared to experimentally determined frequencies that display alignment. The results of this comparison are summarized in Table 2.1. Often a small adjustment compared to the theoretical frequency is needed to obtain good alignment of the CNTs. The small discrepancy between theory and experiment is likely due to the uncertainty in the measurement of d, the potential

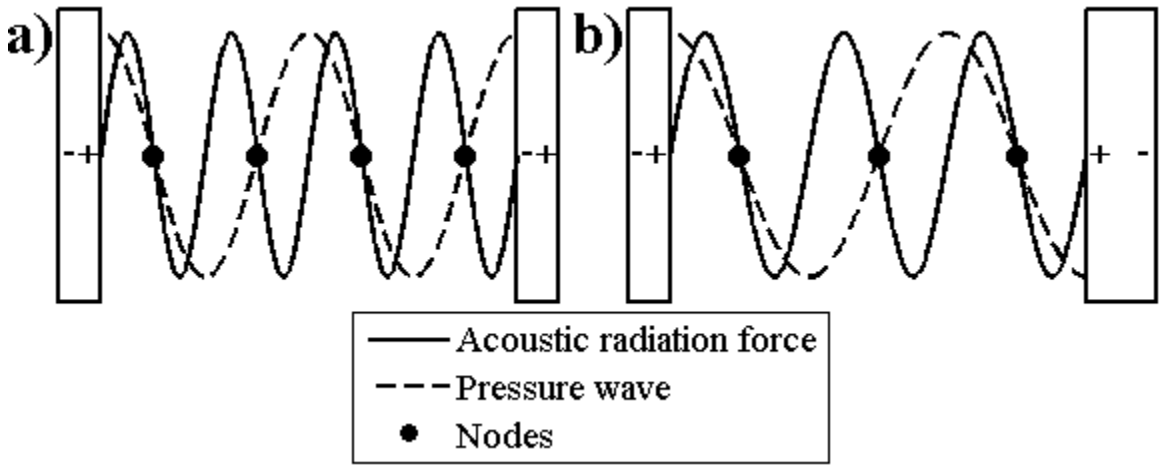

Figure 2.6: PZT polarity setup at a fixed separation to establish an a) even number of nodes and b) odd number of nodes

Table 2.1: Comparison of the predicted frequencies to the observed frequencies that create alignment of CNTs

Nodes	Predicted frequency [MHz]	Actual frequency [MHz]	% Difference
15	0.796	0.779	2.2
17	0.903	0.895	0.9
19	1.009	1.015	0.6
21	1.115	1.135	1.8
23	1.221	1.255	2.7
25	1.327	1.375	3.5
27	1.433	1.495	4.1

misalignment of the PZT plates, and the change in the sound speed in water with increasing temperature caused by the heat generation in the PZT piston source. However, the percent difference, calculated as the ratio of the absolute value of the difference between the theoretical and actual frequency to the theoretical frequency, never exceeds 4.1%.

The expected distance between nodes is $\lambda/2$, two nodes per wavelength as shown in Fig. 2.2. This theoretical prediction is compared to experimental results by means of two independent methods, using water as the host medium. The first method is to align CNTs in water at a frequency of 1.487 MHz and allow the water to evaporate, thus depositing the CNTs on the base of the reservoir. The alignment is confirmed by visual inspection and the expected distance between nodes for this sample is $\lambda/2 = c/2f = 503$ μm, with $c = 1495$ m/s. The sample is imaged using an SEM and the distance between nodes is measured to be 529 μm, as shown in Fig. 2.7a). Upon close inspection of the experimental result, the prediction appears to be a slight overestimate to the actual distance between nodes. The second method involves imaging the orientation of CNTs in

water using an optical microscope at a frequency of 1.135 MHz. The CNTs are shown in black, the image is overlaid with gray lines in the theoretically expected nodal locations (Fig. 2.7b)) and a visual comparison is then performed. Both methods show good agreement between theory and experiment and demonstrate that CNTs can be manipulated in water using BAWs.

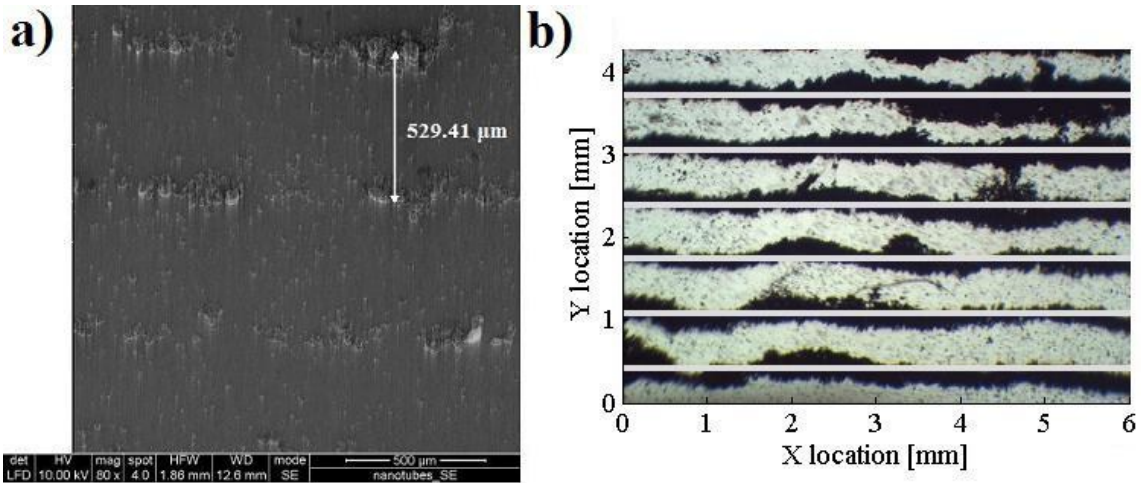

Figure 2.7: Comparison of experimental to theoretical distance between nodes of the standing pressure wave using a) SEM b) optical microscope

CHAPTER 3

EXPERIMENTAL APPARATUS

Figure 3.1 shows a schematic of the apparatus used to fabricate the composite materials tested in this study. It consists of a dog-bone shaped reservoir with two PZT plates rigidly mounted parallel to each other on the side walls of the reservoir. The PZT plates span the entire gauge length of the dog-bone shape. The reservoir is temporarily fixed to a rigid glass slide which provides a removable base that aids in the extraction of the manufactured composite material samples from the reservoir.

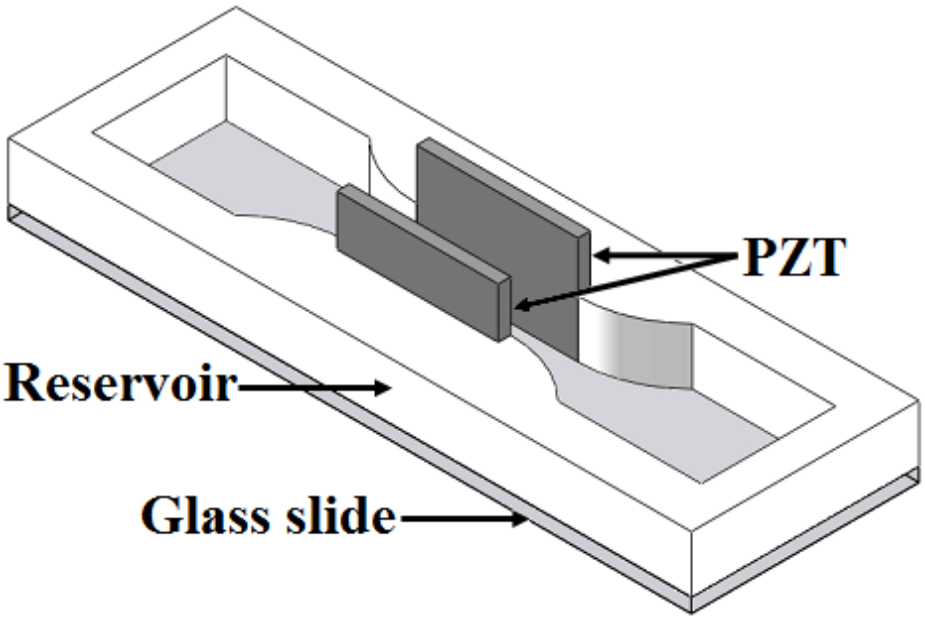

Figure 3.1: Experimental apparatus

The dog-bone shaped reservoir is machined from stock high density polyethylene (HDPE), selected for its limited surface adhesion [95] to the polymer, which allows easy evacuation of the finished composite material samples from the reservoir. Recess slots are cut to fit the PZT plates as shown in Fig. 3.1 and a fully dimensioned schematic of the reservoir is shown in Fig. 3.2. The dimensions of the test samples produced in this reservoir are similar to those of an ASTM D638 Type V plastic sample. The gauge length and width of the sample are 18 mm and 7.5 mm, respectively. This is an increase to the dimensions of the ASTM sample that are 9.53 mm and 3.18 mm, respectively. The dimensions were chosen to provide ample space for the alignment of CNTs based on the resonance frequency of the PZT material and the corresponding wavelength in the host medium. These dimensions can be scaled based on the resonance frequency of the PZT material, the frequency range of the available power amplifier, and the properties of the resin (host medium), without compromising the successful manipulation of CNTs.

The PZT plates are made from PZT-4 material and are operated in the so-called 33 mode as indicated in Fig. 3.3. The properties of the PZT plates are explained here and the values are summarized in Table 3.1. The resonant frequency is the frequency at which the PZT is most efficient at converting electrical energy into mechanical energy or vice versa [96]. The electromechanical coupling factor and the piezoelectric constant are defined for each actuation mode of the PZT (see [97] for a complete description of these modes). The electromechanical coupling factor for the 33 mode of a thin plate, k_t, is the ratio of the electrical energy converted into mechanical energy to the electrical energy supplied. The piezoelectric constant for the 33 mode, d_{33}, represents the amount of expansion/contraction induced per unit voltage [96].

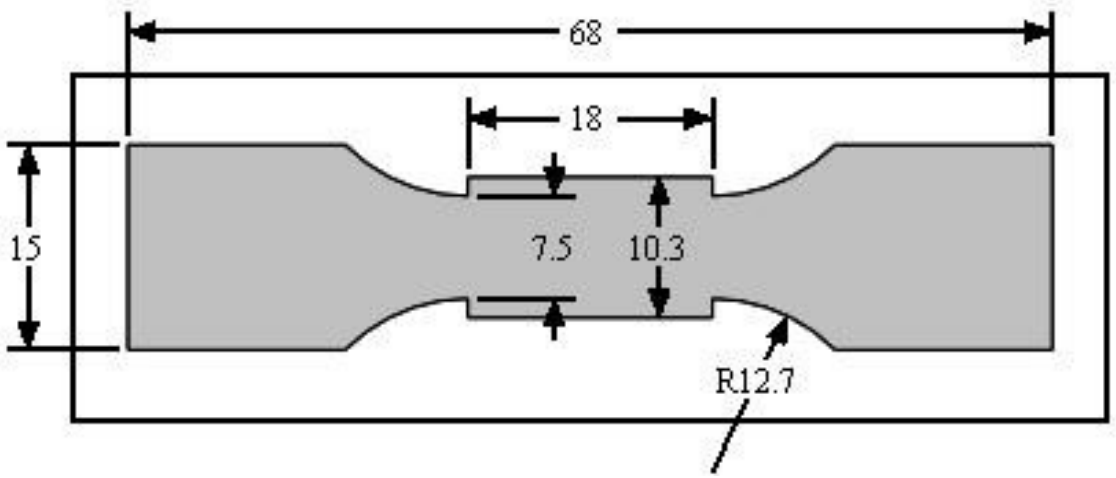

Figure 3.2: Top view of the reservoir with dimensions in millimeter

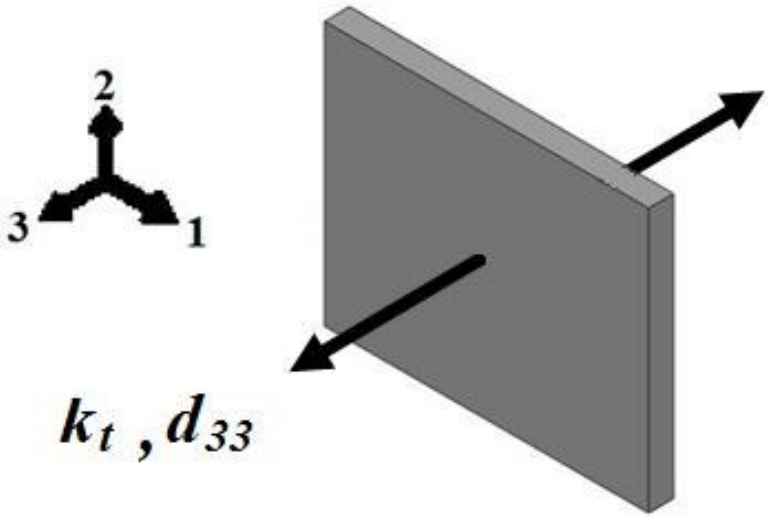

Figure 3.3: Direction of the expansion/contraction of the PZT for determining k_t and d_{33}

Table 3.1: Properties of the PZT plates used in the apparatus [104]

Parameter	Value	Units
Resonant frequency, f_r	1.5	MHz
Electromechanical coupling factor, k_t	0.45	-
Piezoelectric constant, d_{33}	320×10^{-12}	m/V
Quality factor, Q_m	1800	-

The mechanical quality factor, Q_m, is defined as the ratio of the resonant frequency to the span of frequencies that maintain the same admittance and is equivalent to the inverse of the mechanical loss in the PZT plate [98]. PZT material with a high quality factor will have a sharp resonance peak (a short frequency span) and will display low mechanical loss, indicating that less heat is produced within the plate.

The PZT is cut to dimensions of 18 x 12 mm using a diamond precision saw (Allied High Tech Products, Tech Cut 4). A 24 GA wire is soldered to each face of the PZT (these are not shown in Fig. 3.1) to supply the alternating current, which produces the expansion and contraction of the PZT that in turn launches a bulk pressure wave in the host fluid in the reservoir. An arbitrary function generator (Tektronix, AFG 3102) is used as the current source, amplified by a 45 dB 50 W RF power amplifier (Electronic Navigation Industries, 440LA).

Smooth-Cast 300 (Smooth-On, Inc) thermoset resin is used as the matrix material to fabricate all composite material samples in this work. Its properties are listed in Table 3.2. This is a fast curing (3 minutes if performed at room temperature), ultra-low viscosity, polyurethane two part liquid resin that is mixed at a 1:1 volume ratio to initiate the curing process. This fast cure time is required to maintain the alignment of the CNTs during cross-linking of the resin. The choice of resin is vital to the success of ultrasound manipulation of particles (see Chapter 4). It must possess a very low viscosity, cure rapidly, and have a constant sound speed over a wide temperature range.

The carbon nanotubes used in this work are MWNTs (CheapTubes.com). Their specifications are listed in Table 3.3 and an SEM image of the tubes is shown in Fig. 3.4. These CNTs are produced using the catalytic chemical vapor deposition (CCVD) method.

Table 3.2: Properties of the Smooth-Cast 300 resin [105]

Parameter	Value	Units
Pot life @ 23° C	3	min
Cure time @ 23° C	10	min
Tensile strength	3,000 (21)	psi (MPa)
Tensile modulus	139,500 (962)	psi (MPa)
Elongation at break	5	%
Mixed viscosity	80	cps

Table 3.3: Properties of the MWNTs [106]

Parameter	Value	Units
Outer diameter	50-80	nm
Length	10-20	μm
Bulk density	0.18	g/cm^3
True density	2.10	g/cm^3

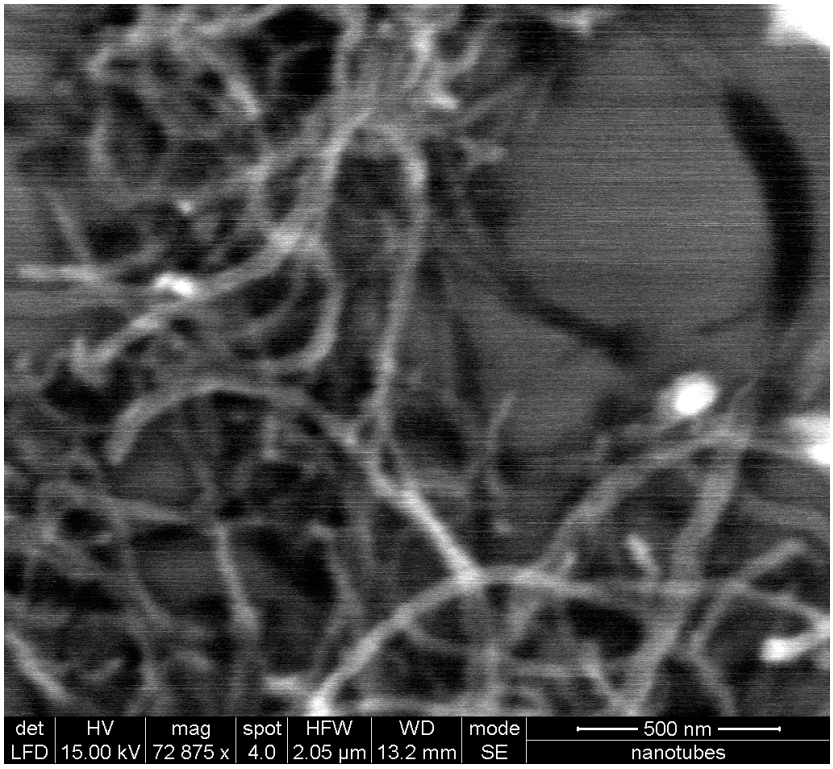

Figure 3.4: SEM image of the CNTs purchased from CheapTubes.com

The CNTs are distributed in a powder form that is subsequently measured by weight on a digital scale (accurate to ± 0.001 grams) before being dispersed in the resin. The length efficiency factor of these CNTs is 0.995, which is satisfactory for use as a filler material [11].

As observed from Table 3.3, two densities characterize the MWNTs; bulk density and true density. The bulk density does not account for the volume of air that is trapped on the surface or on the interior of the CNTs. As such, the bulk density is much lower than the real density of the tubes. A more precise measurement of the volume (and therefore the density) is obtained using a pycnometer device which utilizes Archimedes' principle of fluid displacement with a gas (typically helium) that can penetrate the small gaps a liquid cannot [99]. This volume measurement is much more accurate and is used to calculate the true density. The difference between densities is significant when determining the volume percent (vol%) of CNTs in a composite material.

CHAPTER 4

MANUFACTURING METHOD

The process of creating composite materials with aligned CNTs using the acoustic manipulation method, involves three distinct steps: 1) sound speed measurement, 2) alignment verification, and 3) sample fabrication. The first and second steps only need to be performed once per resin and apparatus, respectively. The third step can be repeated to produce the desired number of samples.

4.1 Sound speed measurement

The sound speed c in the host medium must be known to predict the frequency that will establish a standing pressure wave in the reservoir using Eq. (2.1). The sound speed measurement is performed using a "time-of-flight" approach previously demonstrated in the literature [100]. The setup includes a function generator, an oscilloscope, and a reservoir with two opposing, parallel PZT plates, as shown in Fig. 4.1. The reservoir is filled with the viscous host medium of interest and a pulse signal from the function generator is used to launch a bulk pressure wave that propagates from one PZT plate toward the other PZT plate at the sound speed of the medium. The time-of-flight t is measured by the oscilloscope and the sound speed is calculated as $c = d/t$, with d being the known distance between the PZT plates.

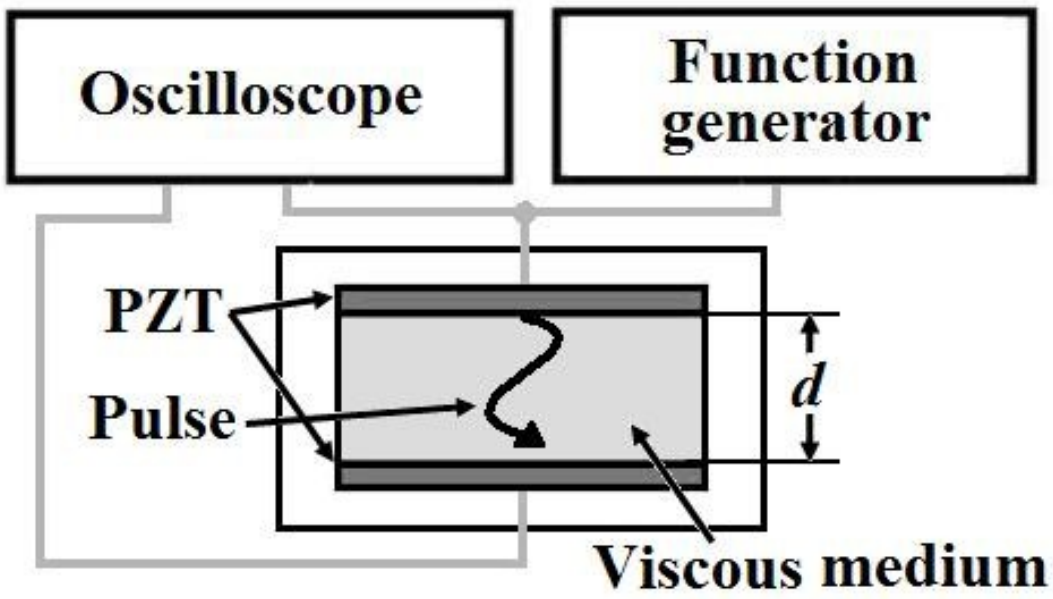

Figure 4.1: Setup to measure the sound speed in viscous media

To verify the accuracy of this method, the sound speed of water and isopropyl alcohol was first measured. The sound speeds of these liquids are well-known and published in the literature. The measured values are within 1% of the published values, indicating that the method can be used to accurately determine the sound speed in viscous media. The results of the performed measurements, including that of the Smooth-Cast 300 resin, are shown in Table 4.1.

Table 4.1: Sound speed measurement results for different viscous media

Medium	**Published sound speed [m/s] [100]**	**Measured sound speed [m/s]**
Water	1506	1495
Isopropyl alcohol	1170	1172
Smooth-Cast 300	-	1353

4.2 Alignment verification

Alignment verification is performed by introducing < 0.50 wt% CNTs into the resin and minimally dispersing them in the resin to maintain optically detectable aggregates of CNTs. The mixture is introduced into the reservoir and the function generator is set to the frequency closest to the resonant frequency of the PZT plates that will establish a standing wave (Eq. 2.2). The amplitude is set to 250 millivolt peak-to-peak (mVpp) and the frequency is adjusted in small increments until alignment occurs as shown in Fig. 4.2. This frequency is used to produce all parts in the reservoir.

4.3 Sample fabrication

The reservoir is prepared before the fabrication of each specimen by cleaning the PZT plates to guarantee a smooth surface and by inserting an anti-stiction layer between the reservoir and the glass slide that forms the removable base of the reservoir. These two steps minimize the adhesion of the resin to the PZT plates and the glass slide during the cross-linking of the resin which reduces the likelihood of damaging the reservoir when removing the cross-linked composite material specimen.

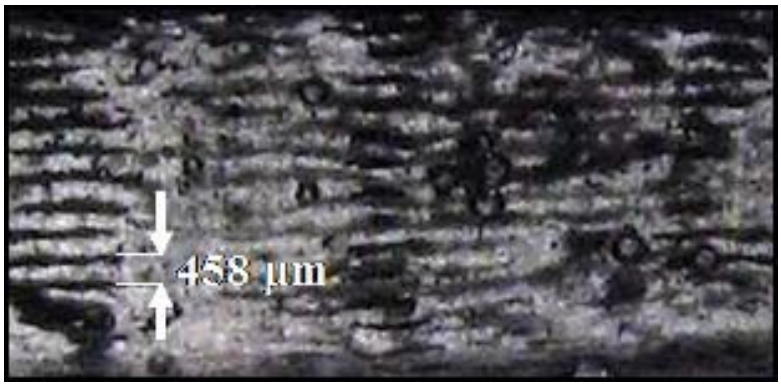

Figure 4.2: Observed alignment of CNTs in the liquid resin using a 1.477 MHz frequency at amplitude of 250 mVpp with the distance between lines indicated

The CNT-resin mixture is formed by adding 2.5 cc (half the volume of the reservoir) of one part of the resin to a mixing cup. The appropriate amount of CNTs to obtain the desired wt% is weighed and added to the resin. The mixture is stirred briefly by hand prior to bath sonication at 42 kHz and 35 Watts for 380 seconds (Blazer Products Inc., 3800-A). Sonication is the simplest, most convenient, and most economical way of dispersing CNTs [60]. After sonication, 2.5 cc of the other part of the resin is added and stirred until the two parts are well mixed. The CNT-resin mixture is then poured into the dog-bone shaped reservoir.

The alignment of the CNTs is achieved by exposing the mixture to the standing pressure wave. Cross-linking of the mixture starts immediately following the addition of the second resin part to the mixture and when the resin becomes "tacky" the standing pressure wave is removed. After complete cross-linking of the resin, the glass slide is removed and the hardened sample is extracted using a punch and die as shown in Fig. 4.3. The anti-stiction layer is then peeled away from the cross-linked composite material.

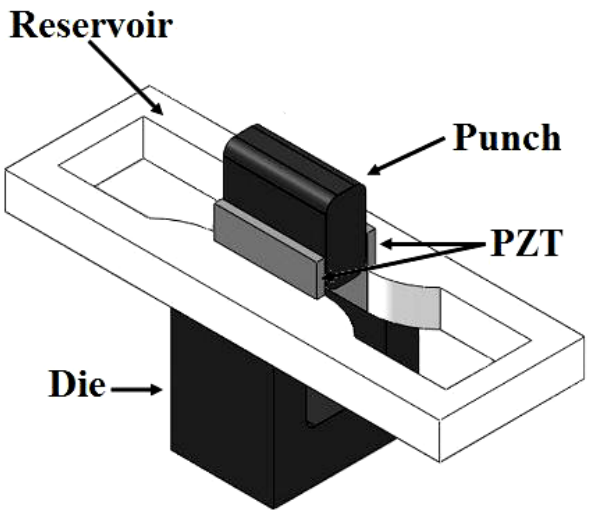

Figure 4.3: Schematic of the extraction technique to evacuate the composite material specimen from the mold using a die punch

This completes the formation of a composite material with aligned CNTs as filler material. A 1 wt% sample formed using this method is displayed in Fig. 4.4 and the alignment of CNTs can be observed in the gauge length of the sample.

4.4 Operating domain and limitations

There are several parameters that can be varied in the formation of these composites materials with aligned CNTs, including the frequency and amplitude of the pressure wave used for alignment of the CNTs, the exposure time of the resin-CNT mixture to the acoustic radiation force, the duration of bath sonication, and the loading rate of CNTs. The operating range for each parameter in this study is summarized in Table 4.2.

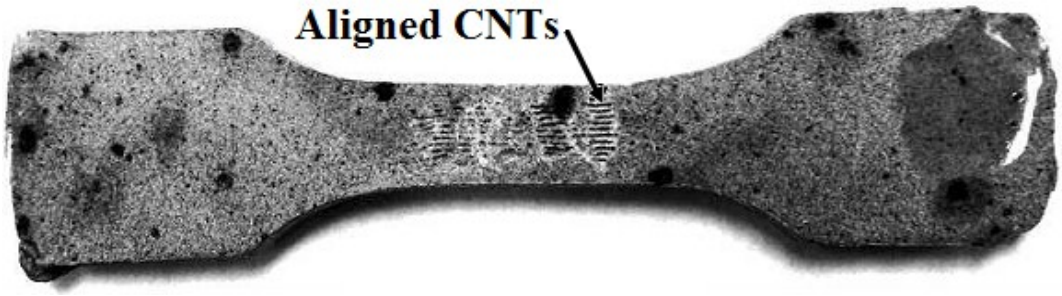

Figure 4.4: Composite material specimen with aligned CNTs (1 wt% loading rate) showing aligned CNTs in the gauge length of the dog-bone sample

Table 4.2: Range of parameters used for the manufacturing method

Parameter	Range	Units
Frequency	1.44-1.48	MHz
Amplitude	200-250	mVpp
Acoustic radiation force exposure	30-90	s
Bath sonication duration	380	s
CNT loading rate	0-2	wt%

The frequency range is determined such that a standing wave can be created in the host medium for the alignment of the CNTs. Only the frequency closest to the resonance of the PZT plates is used to apply maximum power. The amplitude range is determined such that it is large enough to overcome the attenuation of the host medium as well as the drag acting on the CNTs, yet small enough to avoid acoustic streaming. The acoustic radiation force is applied only until the cross-linking of the resin becomes apparent. In our experiments this was achieved after less than 90 seconds. The CNT loading rate is determined such that the acoustic radiation force is effective at manipulating the CNTs. Increasing the CNT loading rate increases the viscosity of the mixture [54]. This increase severely limits the effectiveness of the acoustic manipulation technique to align CNTs because it increases the drag on each CNT. Samples were successfully manufactured using the discussed acoustic manipulation technique up to CNT loading rates of 2 wt%.

CHAPTER 5

RESULTS AND DISCUSSION

Three types of specimens are fabricated: pure resin materials, composite materials with randomly oriented CNTs, and composite materials with aligned CNTs. The specimens are also fabricated with four different CNT loading rates: 0.15, 0.5, 1, and 2 wt%. These loading rates are chosen throughout the CNT loading rate operating range (Table 4.2). Five samples were created for each specimen type and loading rate, respectively. Some samples were removed from the analysis primarily due to air bubbles being entrapped in the composites as a result of the fabrication process. The final number of samples tested of each specimen type and loading rate is summarized in Table 5.1.

The composite samples are tested for alignment, dispersion, and mechanical properties. The alignment obtained in the composite materials, with this new technique, is first quantified and compared to other methods. The level of dispersion obtained in the composite materials is quantified using a dispersion index developed in this work that improves upon the ASTM standard. Finally, the mechanical properties (elastic modulus E_c , ultimate tensile strength σ_{UTS}) of the samples are evaluated using tensile testing. The pure resin materials and the composite materials with randomly oriented CNTs provide two benchmarks against which the composite materials with aligned CNTs are compared.

Table 5.1: Types and quantities of CNT composite material specimens analyzed in this work

CNT loading rate (wt%)	0	0.15	0.50	1.00	2.00	Total
Aligned	-	5	4	2	3	14
Random	-	5	5	3	3	16
Total	9	10	9	5	6	39

5.1 Degree of alignment

The Hermans' orientation factor H [101] is used to quantify the alignment obtained with the acoustic manipulation technique. Although this is a 2D measurement, this factor has been applied to CNT-polymer composites in many instances [37, 102-104]. H is computed using Eq. (5.1) based only on the average angle between the fiber axis and the composite axis ϕ. The composite axis is defined as the axis in which alignment is desired, and in which the load will be applied. Equation (5.1) is plotted in Fig. 5.1 and shows that perfect alignment results in $H = 1$ ($\phi = 0°$). Perfect misalignment, defined as all fiber axes being oriented perpendicular to the composite axis ($\phi = 90°$), results in $H = -0.5$. Random alignment results in $H = 0.25$ ($\phi = 45°$)

$$H = \frac{1}{2}(3\cos^2\phi - 1) \tag{5.1}$$

This factor is determined for five composite material samples to quantify the macroscale alignment of CNT clusters. It is performed by photographing a 6.7 by 5.0 mm section of the aligned CNTs using a 5.0 MP camera mounted to a trinocular stereo zoom

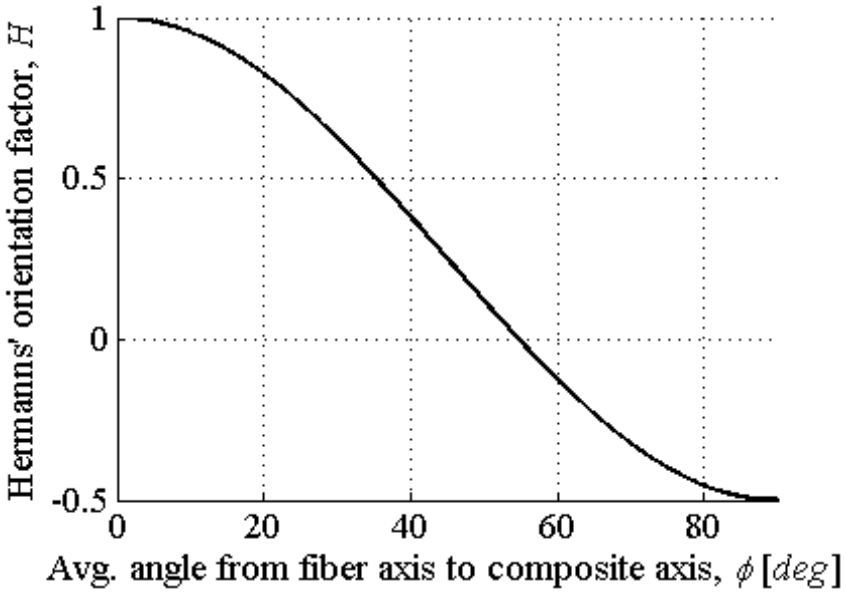

Figure 5.1: Hermans' orientation factor H versus average angle between the fiber axis and the composite alignment axis ϕ

microscope (AmScope, MT500). These digital images are converted into binary images using a luminance cut off of 0.20, creating an image with white resin and black CNTs. The image is then overlaid, by hand, with gray lines through each CNT cluster axis. Figure 5.2 displays both the raw and final images for a 1 wt% sample. ϕ is computed as the average angle between all lines and the vertical (composite axis) in the image. Special care was taken to ensure that the sample was aligned vertically. H is finally calculated using Eq. (5.1) and the results for the five samples (representing three wt%) are given in Table 5.2. The average orientation factor of the five samples is determined to be 0.988. Even though this represents a macroscale alignment factor, it nevertheless demonstrates excellent alignment of the CNTs.

The CNT filler material is nanosized and, thus, alignment should also be assessed on the nanoscale. To accomplish this, a < 0.01 wt% aqueous solution of CNTs is bath sonicated for 8 minutes and subsequently aligned using the described BAWs technique.

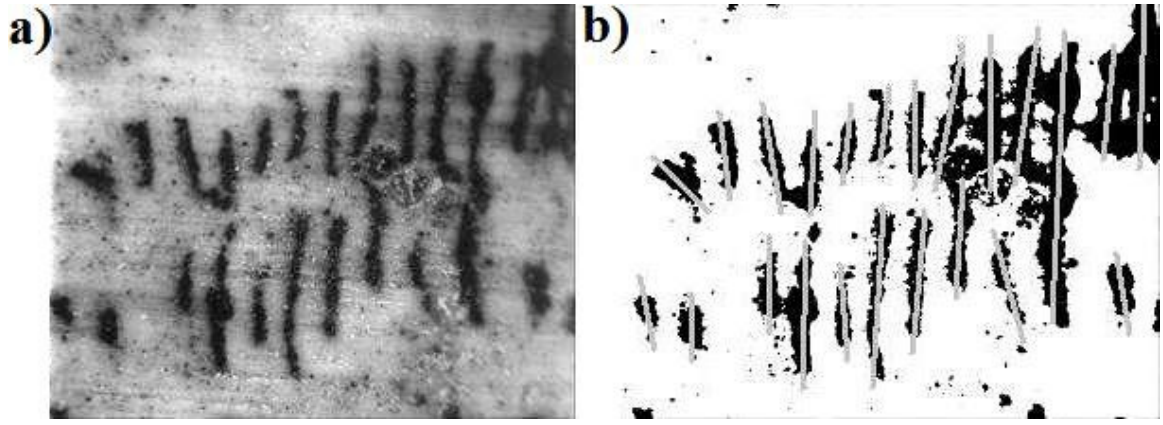

Figure 5.2: Microscale alignment, a) unprocessed image and b) processed image showing black CNT clusters overlaid with gray lines along their axis for determining the Hermans' orientation factor of a specimen

Table 5.2: Hermans' orientation factor results obtained for five samples

Sample	ϕ [deg]	H
0.50 wt%	2.51	0.997
1.00 wt%-a	7.38	0.975
1.00 wt%-b	3.45	0.995
2.00 wt%-a	5.02	0.989
2.00 wt%-b	5.66	0.985
Average	4.80	0.988

The water is allowed to evaporate, depositing the aligned CNTs on the glass base of the reservoir. The glass slide is then imaged using an SEM at a magnification level of 500 nm and 50 μm. At the 500 nm magnification, individual MWNTs are distinguishable and at the 50 μm magnification, a clear image of a single nodal line is obtained. These images are overlaid with gray lines as before to determine the Hermans' orientation factor. The processed images are shown in Fig. 5.3. The nanoscale image (500 nm magnification) shown in Fig. 5.3a) definitely displays some CNTs that are not in good alignment

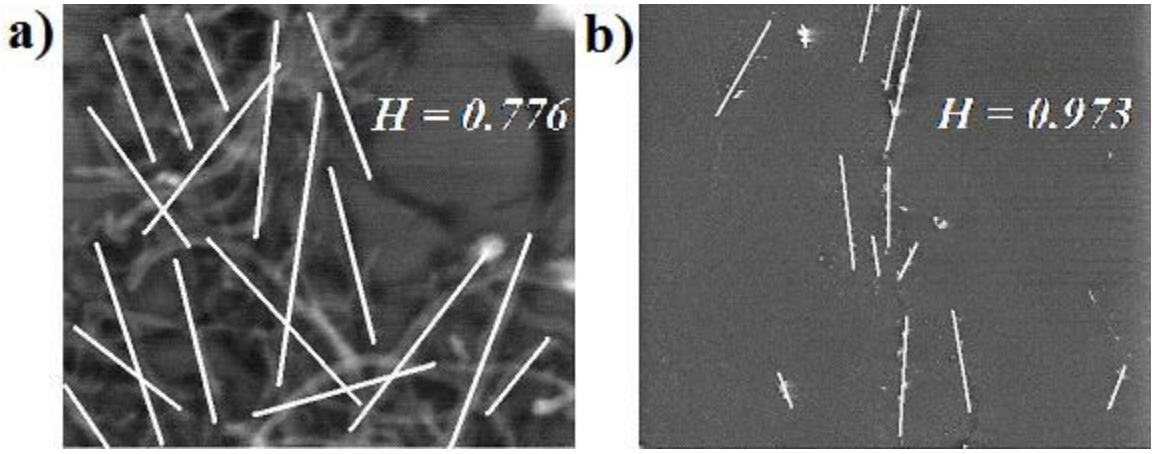

Figure 5.3: Processed SEM images at a) 500 nm and b) 50 μm magnification levels to calculate a Hermans' orientation factor

However, an alignment factor of $H = 0.776$ is obtained. This is in the range of values reported in the literature for other CNT alignment methods such as mechanical stretching (H of approximately 0.70) and wet spinning ($H = 0.85$) (see appendix). The microscale image shows overall alignment identical to the macroscale images with $H = 0.973$. These images show that even on the nanoscale, a high degree of alignment is obtained with the acoustic manipulation technique. It is also speculated that the nanoscale alignment would improve even further if shorter CNTs are used. Shorter CNTs are less likely to entangle (as shown in Fig. 1.4), thus facilitating manipulation.

5.2 Degree of dispersion

The standard for quantifying the dispersion of carbon black in a compound is outlined in ASTM D2663-08. This method has three test methods; a visual inspection (Method A), a microscopic agglomerate count (Method B), and a surface roughness measurement (Method C). The agglomerate count method, used previously for CNT composites [65, 105], will be compared to a new method developed for this study. The

fabricated samples outlined in Table 5.1 will then be quantified using the new method.

The ASTM standard mandates dividing the test-image into nine equal-sized fields as shown in Fig. 5.4a). Each of these nine fields is further divided into 10,000 squares that, under proper magnification, are 10 x 10 μm in size for a total of 90,000 squares. A count of all squares that are at least half full of carbon is performed for only five of the nine fields. The four arbitrarily eliminated fields are indicated in gray in Fig. 5.4a). This count is divided by five to obtain an average of the five fields, and is assigned the variable *U*. The dispersion index *D* is calculated using Eq. (5.2) where *L* is the volume percentage (0-100) of carbon and *S* is the swelling factor (only used for rubber compounds and considered equal to 1 here). The range of this index is [0,100] with 100 indicating perfect dispersion. Up to this point in the thesis, the amount of CNTs in a composite has been characterized by a wt% loading rate. Because the ASTM standard requires a volume percentage (vol%) based on the bulk density of the carbon, the vol% will now be used along with wt% for characterizing the amount of CNTs in a composite sample.

$$D = 100 - \frac{SU}{L} \tag{5.2}$$

Quantifying the dispersion of carbon in a compound involves two primary factors: the dispersion distribution of particles (how well spread out the carbon is) and the size distribution of particles (how large the carbon agglomerates are) throughout the sample.

The ASTM dispersion index is limited in its ability to measure these two factors.

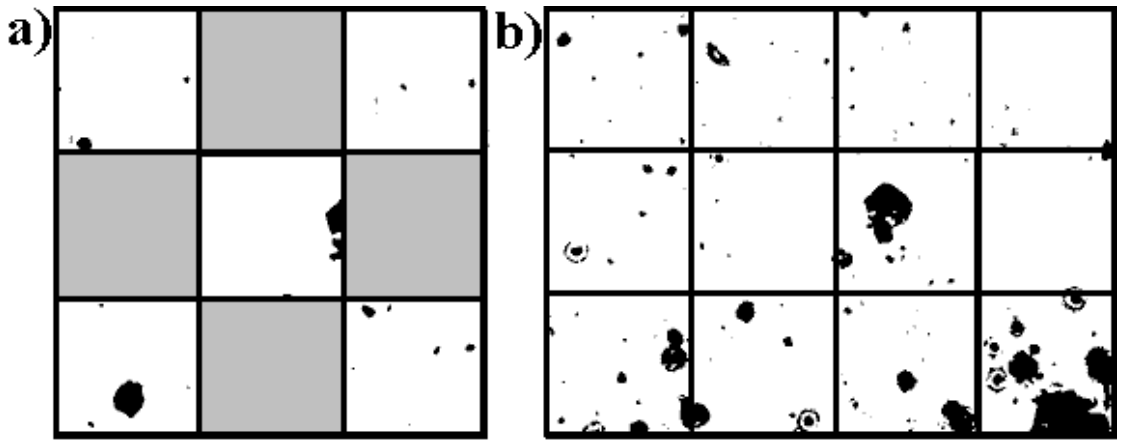

Figure 5.4: Comparison of the dispersion index calculation for a) the ASTM standard and b) the index developed in this work

First, it does not consider the distribution of carbon over the entire sample. This is because it does not compare the amount of carbon between fields, but rather calculates an average over all fields. Second, it does not take into account the size of particles; it assumes that they are smaller than 10 μm. Finally, the index arbitrarily eliminates four of the nine fields it defines, the inclusion of which could substantially alter the resulting index. It is therefore necessary to develop an index better suited for quantifying the dispersion of CNTs in a composite material.

The composite dispersion index *compIndex* developed in this work includes two indexes: the dispersion distribution index *dIndex* and the size distribution index *sIndex*. These two indexes account for the two primary factors that quantify dispersion. Each index has two parts, one part relates to the shape of the distribution and the other part relates to the span of the distribution.

The dispersion distribution index is determined using a 3 x 4 grid as shown in Fig. 5.4b), chosen to coincide with the aspect ratio of standard images. In contrast to the ASTM standard, the newly developed index accounts for all fields in the image. The grid

size is chosen to be large enough to avoid one square being entirely filled with carbon yet small enough to be sensitive to the concentration between fields. The dispersion distribution index is calculated using Eq. (5.3) where b is the set of carbon black percentages for the 12 fields of the grid, $s(b)$ is the standard deviation of b, and $\bar{b}$ is the arithmetic average of b. The constant 0.5222 is the largest possible standard deviation for 12 numbers that range from 0 to 1, namely the set of six zeros and six ones. The formula accounts for the shape of the dispersion distribution with the standard deviation, and the span of the distribution with the ratio of the average concentration to the maximum concentration. The range of the index is [0, 1] with 1 indicating perfect dispersion.

$$dIndex = \frac{1}{2}\left[1 - \frac{s(b)}{0.5222} + \frac{\bar{b}}{\max(b)}\right] \tag{5.3}$$

The size distribution index calculation must be performed without a grid since large particles are likely to cross grid boundaries. The area of each particle in the image is determined using a computer algorithm by counting the number of pixels occupied by each particle, and *sIndex* is the calculated using Eq. (5.4). Here, a is the set of all particle sizes, N is the total number of particles and l is the number of particles whose area is less than a threshold of 100 pixels. The threshold was selected to be independent of the vol% CNTs in the sample, to make the resulting index independent of the expected carbon concentration. Thus, the index determines how well the observed carbon is distributed across the image and disregards the total amount of carbon. The value of 100 was the maximum particle size for images with randomly generated dispersion up to a vol% of 20

(4 wt%). This makes it possible to achieve a perfect dispersion rating over a wide range of carbon concentrations. The index accounts for the size distribution with the threshold count, and the span of the size distribution with the ratio of the maximum area to the total area. The range of the index is [0, 1] with 1 being assigned to an image with no observed particles, this would mean the agglomerates of CNTs are too small to be detected in the image.

$$sIndex = \frac{1}{2}\left[\frac{l}{N} + 1 - \frac{\max(a)}{\sum a}\right] \tag{5.4}$$

The composite index *compIndex* is calculated as the arithmetic average of the *dIndex* and the *sIndex* but the two separate indexes should still be reported to better characterize the dispersion. The new index is compared to the ASTM standard using two tests: a benchmark test and a sample test. The benchmark test utilizes three computer generated images shown in Fig. 5.5, all of which are 5 vol% (0.9 wt%) images. Figure 5.5a) is a random distribution of carbon; Figs. 5.5b) and 5.5c) are identical aggregates in different locations on the image. The sample test utilizes three images from composite materials with randomly dispersed CNTs fabricated for this work and shown in Fig. 5.6. They represent three different CNT loading rates, 0.5, 1, and 2 wt% corresponding to 2.9, 5.6, and 10.7 vol%, respectively.

The resulting dispersion indexes obtained with both methods are shown in Table 5.3. Recall that the ASTM standard involved a count of squares measuring 10 x 10 μm. The raw images in this analysis have a resolution of 2.5 x 2.5 μm and a larger field of

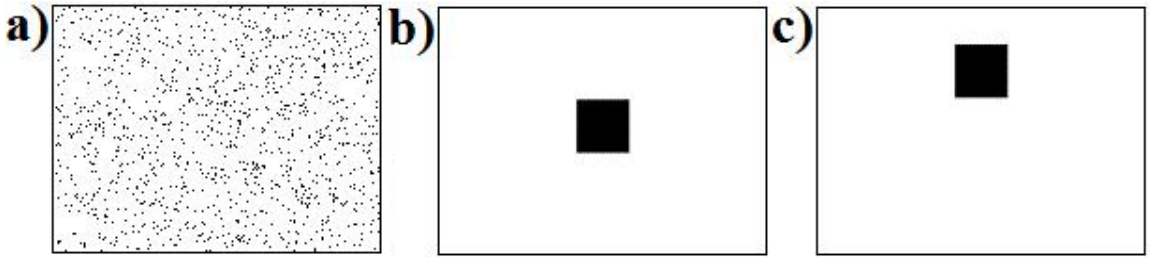

Figure 5.5: Benchmark images used to compare the ASTM index to the new index. a) shows a random computer generated 5 vol% sample, b) and c) show two variations of a 5 vol% sample

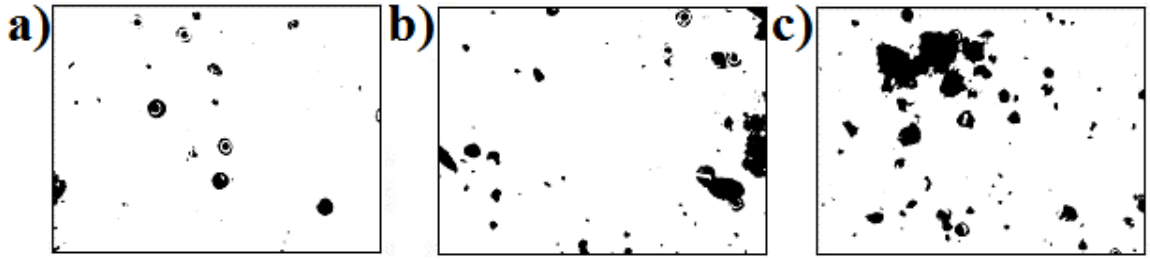

Figure 5.6: Sample images to compare the ASTM index to the new index at 3 different vol% loading rates; a) 2.9% b) 5.6% c) 10.7% vol%, corresponding to 0.5, 1, and 2 wt%, respectively

Table 5.3: Dispersion index results from the ASTM index and the compIndex (dIndex and sIndex) for six test images

Image	**ASTM index (*D*)**	***dIndex***	***sIndex***	***compIndex***
Benchmark a)	100	0.994	0.999	0.997
Benchmark b)	0	0.511	0	0.255
Benchmark c)	100	0.533	0	0.267
Sample a)	54.4	0.677	0.717	0.697
Sample b)	69.6	0.562	0.553	0.557
Sample c)	0	0.479	0.572	0.526

view than what was used in the ASTM method. Hence, these images are first cropped and then analyzed accordingly to match the ASTM standard.

The results from both indexes for benchmark a) show almost perfect dispersion results, as expected for an image with randomly generated black pixels. However, the two indexes differ significantly in their handling of benchmarks b) and c). Even though the samples contain an equal size and dispersion distribution, the ASTM index yields complete opposite results for benchmark b) = 0 and c) = 100. The *compIndex* handles these benchmark images much more consistently, yielding nearly identical results of approximately 0.26, which matches reality. This is a marked improvement over the ASTM standard and exploits the limitation behind excluding fields in the grid.

The results from the sample images also show the limitations of the ASTM index. Visually, the dispersion of the samples should rank a) best and c) worst. While the compIndex follows that visual observation, the ASTM standard does not. It ranks b) as the best. The ASTM index does not consider how closely packed the carbon black is and, thus, the large cluster on the right in sample b) is averaged over the white space in the middle of the image yielding a higher dispersion index than it deserves based on visual observation. The ASTM index ranks c) last with $D = 0$. This value is equivalent to the result found for benchmark b) where all the carbon is concentrated in one location. Sample c) clearly displays better dispersion than benchmark b) but the ASTM index does not detect a difference between both cases. This demonstrates the limited range in which the ASTM index is effective. The compIndex developed here is more versatile and is able to handle dispersions that are poor (benchmark b)) and near perfect (benchmark a)) without losing its ability to quantify the dispersions of actual parts (samples a)-c)).

The compIndex addresses the three limitations to the ASTM index and has been shown to work effectively for both the benchmark test and the sample test. While not a perfect index, it is a marked improvement over the ASTM standard. This index is used to quantify the dispersion of all samples manufactured in this work. This is done by photographing the fracture surface of all tested composite samples (both randomly oriented CNTs and aligned CNTs) and processing them as explained in section 5.1. The fracture surface is used to analyze the dispersion as it is likely the worst dispersion in the sample. Poor dispersion generates voids that weaken the strength of the composite. Here we quantify the dispersion and in the next section discuss its relationship to strength.

As outlined in Chapter 4, dispersion was only performed by bath sonication due to limited resources available. This dispersion technique has been shown to be inconsistent in its ability to disperse CNTs [15]. As a result, the dispersion ratings are found to be rather limited for all samples fabricated with a CNT loading rate in excess of 0.15 wt%. The average dispersion index results for all samples of each loading rate are given in Table 5.4 and the composite index is plotted as a function of loading rate in Figure 5.7. An 18% decrease in the dispersion index is observed from the 0.15 wt% samples to the

Table 5.4: Average dispersion index results for all composite material samples made in this work

CNT loading rate [wt%]	**Average *dIndex***	**Average *sIndex***	**Average *compIndex***
0.15	0.557	0.768	0.663
0.50	0.470	0.613	0.541
1.00	0.443	0.599	0.521
2.00	0.480	0.626	0.553

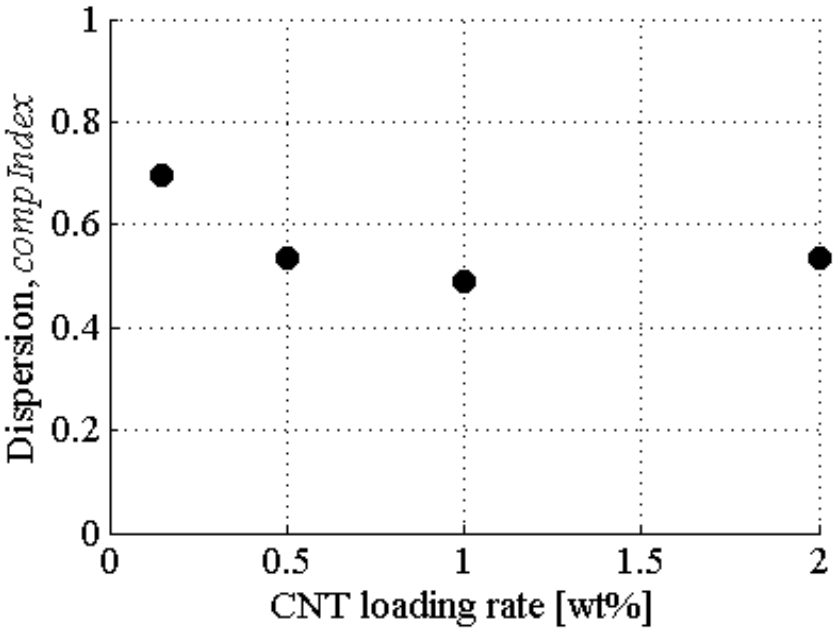

Figure 5.7: Dispersion versus CNT loading rate in wt%

0.50 wt% samples and the dispersion remains low for all other loading rates. This indicates that for effective dispersion bath sonication is limited to very low CNT loading rates.

5.3 Static testing

A primary objective of this study is to measure the change in mechanical properties obtained by the alignment of CNTs in a polymer matrix using BAWs. This is achieved by traditional tensile testing of the dog-bone samples with the compositions described in Table 4.1. The mechanical properties of interest are the elastic modulus E and the ultimate tensile strength $\sigma_{UTS,}$ which are extracted from the tensile test data for each sample. The results obtained for the composite materials with aligned CNTs are compared to both the pure resin material and the composite material specimens with randomly oriented CNTs as benchmarks.

Before testing, each sample is prepared by ensuring that the faces of the samples are flat and that the gauge length of the sample has a uniform cross-section. Thus, each sample is first sanded flat by hand, using a strip of 35 mm wide P60 sandpaper firmly fixed to a flat surface. The sides of the sample along the gauge length are also sanded flat by hand using a separate piece of sandpaper. The cross-sectional area of each sample is measured with calipers and recorded. Visual inspection of the flatness of the sample completes its preparation. Without proper and consistent sample preparation, the tension test could induce a bending load on the sample and the measurement of the cross-sectional area could additionally be inaccurate. Both of these variables can significantly affect the results of the tensile test.

The prepared samples are then installed and tested in a load frame (Instron 5985) as shown in Fig. 5.8. The cross-sectional area of the sample is entered into the control software (Bluehill 3) and the tensile test is performed at a rate of 2 mm/min. Strain readings are performed up to a maximum extension of 1.2 mm using an extensometer

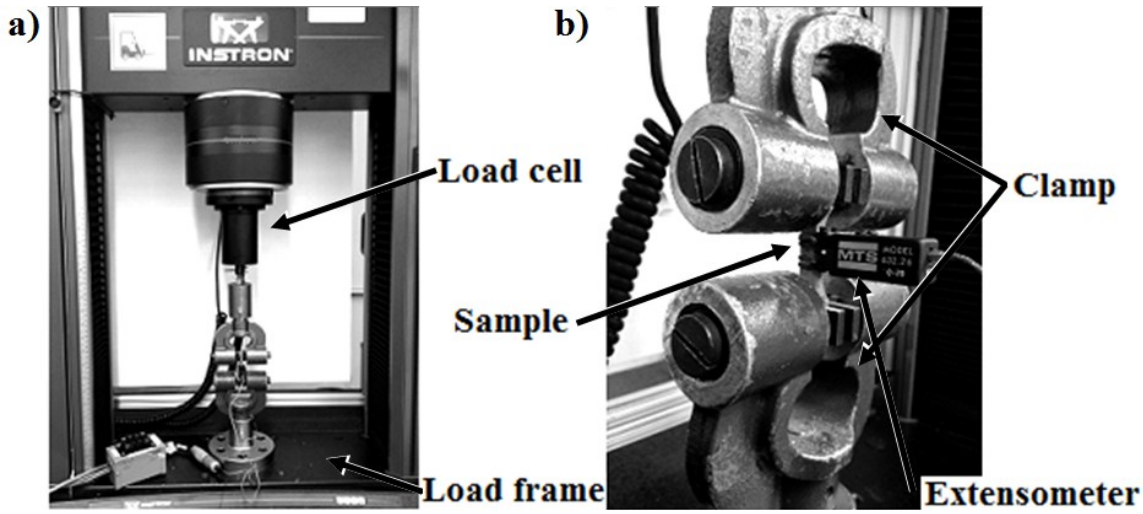

Figure 5.8: Mechanical testing, a) Dog-bone sample installed in the load frame, b) a close up image of the clamped specimen

(MTS 632.26 C-20) with an 8 mm grip spacing while the load is simultaneously monitored using a 1 kN load cell. The sample is loaded until failure with the extensometer being removed as necessary prior to failure. The software computes E_c and $\sigma_{UTS,c}$ for each sample from the stress-strain curve.

The experimental results are normalized by the average ultimate tensile strength $\sigma_{UTS,m}$ and elastic modulus E_m of the pure resin matrix material samples. The arithmetic average and the 90% confidence interval are calculated for each of the specimen types outlined in Table 5.1. The resulting E_c/E_m and $\sigma_{UTS,c}/\sigma_{UTS,m}$ values are plotted in Figs. 5.9 and 5.10, respectively. The data are also tabulated in Table 5.4 to provide the detail that is not easily obtained from the figures.

From Figs. 5.9 and 5.10 it can be observed that the technique of aligning CNTs using BAWs effectively increases the elastic modulus of the composite material. Secondly, increasing the CNT loading rate beyond 0.15 wt% does not seem to result in an increase of the elastic modulus or the tensile strength of the specimens, which indicates that at loading rates > 0.15 wt% dispersion of the CNTs in the matrix material was not fully achieved.

For the 0.15 wt% CNT loading rate, the composites materials with aligned CNTs are 44% stiffer than the composite materials with randomly oriented CNTs, and 51% stiffer than the pure resin materials. For this case, the data show that the 90% confidence interval limits of the composite materials with aligned and randomly oriented CNTs do not overlap. This significant increase in elastic modulus is a clear indication that alignment of CNTs in a composite material improves its mechanical properties as opposed to using a CNT filler material with random orientation.

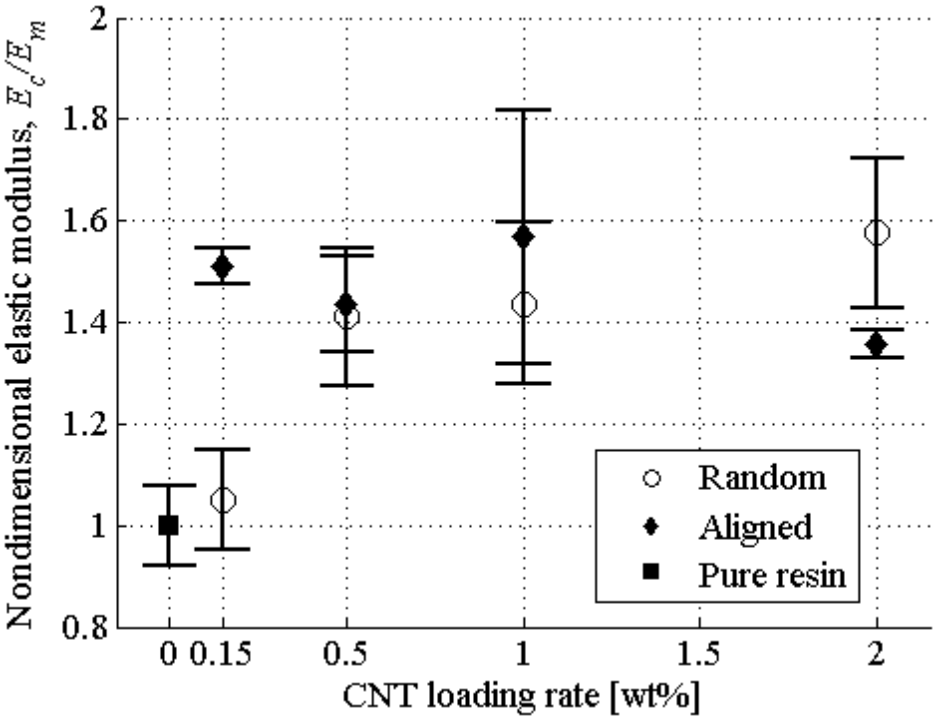

Figure 5.9: Nondimensional elastic modulus results with 90% confidence intervals versus CNT loading rate [wt%]

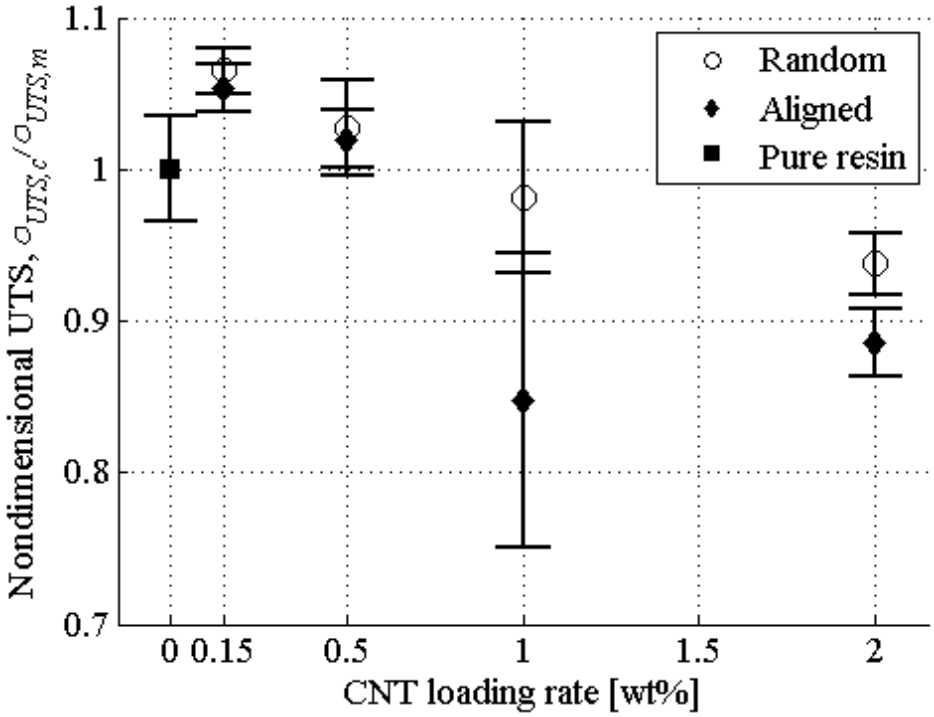

Figure 5.10: Nondimensional ultimate tensile strength results with 90% confidence intervals versus CNT loading rate [wt%]

Table 5.5: Summary of static testing results displayed in Figs. 5.9 and 5.10

CNT loading rate [wt%]	Alignment	Average E_c/E_m / Average $\sigma_{UTS,c}/\sigma_{UTS,m}$	90% confidence interval lower limit	90% confidence interval upper limit
0	-	1	0.92	1.08
		1	0.99	1.01
0.15	Random	1.05	0.95	1.15
		1.06	1.05	1.08
0.15	Aligned	1.51	1.47	1.55
		1.05	1.04	1.07
0.50	Random	1.41	1.28	1.55
		1.03	1.00	1.06
0.50	Aligned	1.44	1.34	1.53
		1.02	1.00	1.04
1.00	Random	1.44	1.28	1.60
		0.98	0.93	1.03
1.00	Aligned	1.57	1.32	1.82
		0.85	0.75	0.94
2.00	Random	1.58	1.43	1.72
		0.94	0.92	0.96
2.00	Aligned	1.36	1.33	1.38
		0.89	0.86	0.91

While the limits of the 90% confidence interval overlap for the CNT loading rates > 0.15 wt%, an increase in elastic modulus compared to the pure resin material specimens is still observed. We speculate that for loading rates > 0.15 wt% dispersion of the CNTs is not fully achieved, resulting in less predictable results for their mechanical properties. Hence, the confidence intervals are the smallest at the 0.15 wt% loading rate.

The theoretically expected increase in elastic modulus for these CNT composite materials can be compared to the experimental results by modifying the Cox model (Eq. (1.1)) to account for the alignment of the filler material. This was performed by Krenchel [51] who added the orientation factor η_o as shown in Eq. (5.5). Other composite models

were considered for comparison but experimental work has found Krenchel's to be the most accurate [106]. Krenchel found that fibers aligned in-plane and random fibers have orientation factors equal to 0.375 and 0.200, respectively. Using Eq. (5.5), the increase in elastic modulus by aligning the filler material can be predicted. E_f was taken to be 1 TPa [48] and the average elastic modulus obtained from the tensile tests of the pure resin specimens was used for E_m. The equation is used to compare the results at the 0.15 wt% loading rate, for which the most significant increase in elastic modulus was obtained, in two ways, 1) to predict the elastic modulus of the composite material with aligned CNTs, and 2) to obtain an effective orientation factor η_o based on the experimental results. The results are normalized by the elastic modulus of the pure resin specimen, similar to Fig. 5.9, and are shown in Table 5.6.

$$E_c = \left(\eta_o \eta_l E_f - E_m\right) V_f + E_m \tag{5.5}$$

The results show that the effective orientation parameter for the aligned composite is 0.469, a 25% increase over the in-plane factor of 0.375. The elastic modulus of the specimens with aligned CNTs is in good agreement with the predicted value.

Table 5.6: Comparison of theoretical and experimental results for the elastic modulus

Specimen Type	E_c/E_m **actual** / η_o **actual**	E_c/E_m **predicted** / η_o **predicted**	**% diff.**
0.15 wt% Random	1.040	1.220	14.80
	0.047	0.200	76.50
0.15 wt% Aligned	1.490	1.410	5.67
	0.469	0.375	25.10

The two results display a less than 6% difference. These results are a clear indication that the fibers have been aligned in-plane as intended using BAWs. The composite material specimens with randomly oriented CNTs show approximately 15% difference between the theoretically expected and the experimentally observed increase in elastic modulus.

The increase in elastic modulus for the specimens with aligned CNTs does not seem to be significant above the 0.15 wt% CNT loading rate. This can also be observed in the ultimate tensile strength results. In fact, loading rates above 0.15 wt% show a steady decline in the ultimate tensile strength of the composite. Results below the tensile strength of pure resin material are found beyond a loading rate of 1.00 wt%. This is likely due to incomplete or insufficient dispersion of the CNTs in the matrix material.

To determine if dispersion is the reason for the observed decrease in the ultimate tensile strength, $\sigma_{UTS,c}/\sigma_{UTS,m}$ is plotted as a function of the dispersion index (*compIndex*) in Fig. 5.11. Included on this plot is a linear fit of the data (solid line), a 90% confidence interval to that fit (dashed lines), as well as indications to images of fracture surfaces of tested specimens displayed in Fig. 5.12. The linear fit indicates that strength increases with increasing dispersion index, confirming our hypothesis. The confidence interval indicates that the dispersion index is not perfectly correlated to the ultimate tensile strength. This is not surprising as other factors play a role as well, such as the strength variation of pure resin, the preparation of the sample, and the proper installation of each sample into the load frame. The sample images show a visual appreciation for the type of dispersion observed. Figure 5.11a) is the highest dispersion rating, a sample with 0.15 wt% randomly oriented CNTs. Figure 5.11b) is the lowest dispersion rating, a sample with 1.00 wt% randomly oriented CNTs. Figures 5.11c) and 5.11d) are visible outliers.

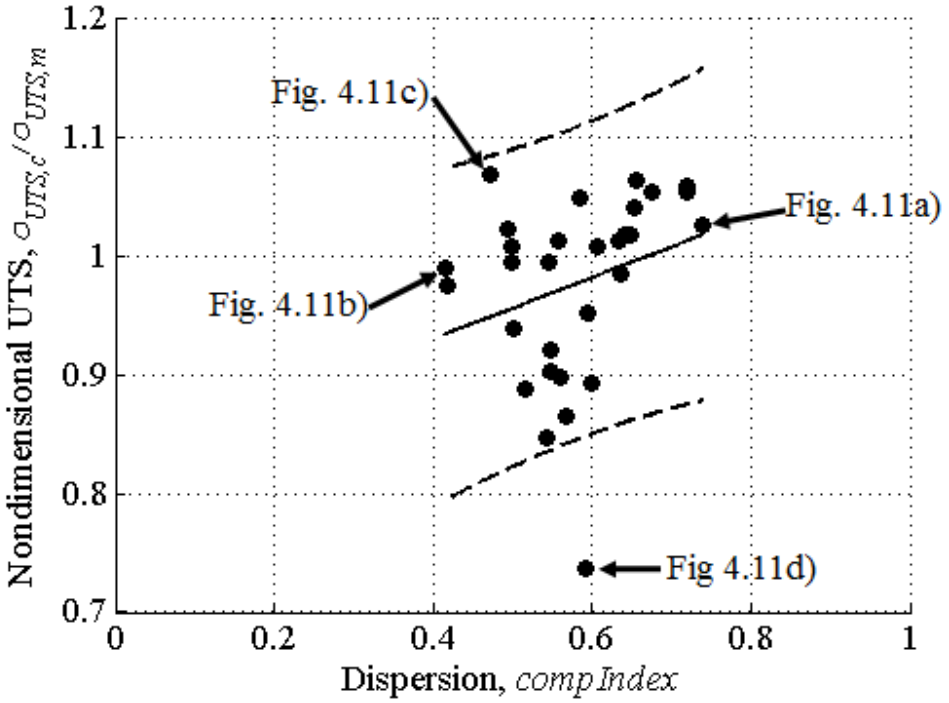

Figure 5.11: Nondimensional ultimate tensile strength version dispersion for all composite material samples. A linear fit and 90% confidence interval are also included

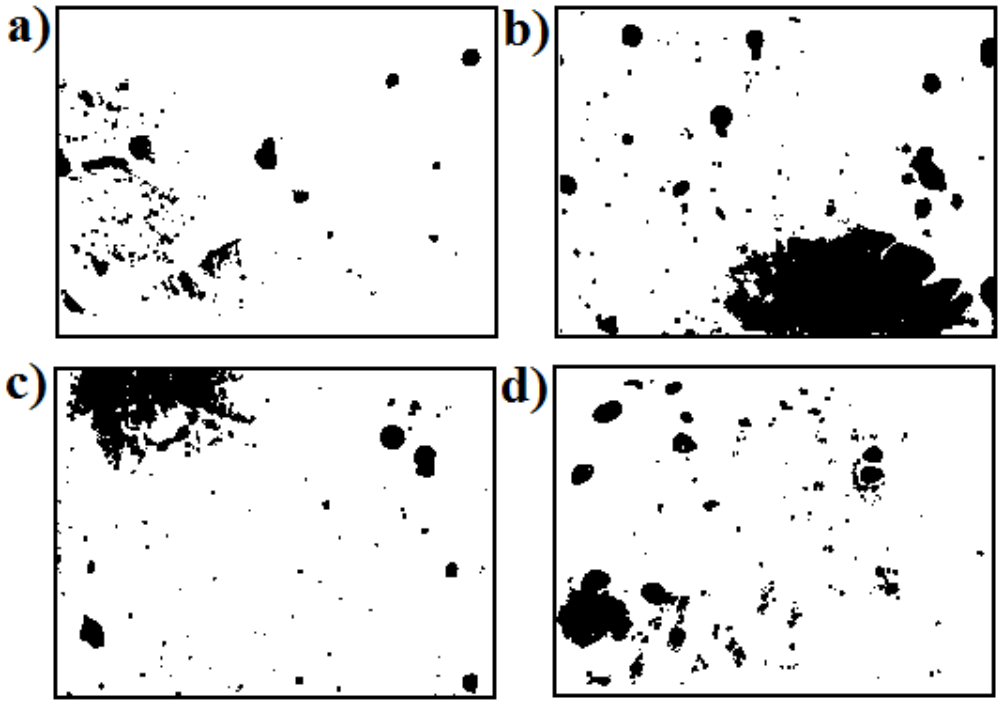

Figure 5.12: Selected fracture surface images processed for dispersion quantification, a) 0.15 wt% with randomly oriented CNTs, b) 1.00 wt% with randomly oriented CNTs, c) 0.50 wt% with randomly oriented CNTs, and d) 1.00 wt% with aligned CNTs

These outliers represent a sample with 0.50 wt% randomly oriented CNTs and a sample with 1.00 wt% aligned CNTs, respectively.

CHAPTER 6

CONCLUSION

Alignment of CNTs in a macroscale volume has been achieved using BAWs. The alignment method, while performed in a small reservoir, can be scaled to produce much larger volumes of composites materials with aligned CNTs by means of using larger PZT plates and a suitable power amplifier. This unique method contributes to the problem of scalable manipulation and alignment of CNTs [29].

There are two primary limitations to this method: 1) the viscosity and cure time of the host medium (thermoset resin), and 2) the final shape of the composite parts. The viscosity of the CNT-resin mixture increases with increasing the CNT loading rate. When 5 wt% is exceeded, the viscosity of the resin creates a drag force on the CNTs that could not be overcome with the instrumentation used in our setup. However, even if the drag could be overcome, it is difficult to achieve good dispersion at this loading rate [107]. The types of resin that can be employed using this acoustic manipulation technique are currently limited to fast curing, ultra-low viscosity thermosets. Several other resins were attempted in this work but demonstrated difficulty in either forming alignment of CNTs or maintaining that alignment through the hardening process. Finally, the shape of the composite material with aligned CNTs is limited to one with two parallel sides for the PZT plates to establish the standing pressure wave. However, this only limits the shape of

the parts that have been directly extracted from the reservoir. The part can be further machined to the desired shape following its removal from the reservoir.

Despite the limitations of this method, the composite material specimens fabricated for this research exhibited near perfect Hermans' orientation factors on the macro and microscale. The alignment on the nanoscale was shown to be comparable to the CNT alignment techniques of mechanical stretching and wet spinning. The composite material samples fabricated using the acoustic manipulation technique, demonstrated an increase in ultimate tensile strength of 5% and elastic modulus of 51% at a CNT loading rate of 0.15 wt% compared to the pure resin material. When further increasing the CNT loading rate, the increase in elastic modulus remained constant while the ultimate tensile strength of the composite material decreased due to poor dispersion of the CNT in the resin matrix material.

The primary advantage to the acoustic manipulation technique to align CNTs over other alignment techniques is its scalability. Most alignment techniques extrude a CNT-polymer mix out from a small diameter needle to perform the alignment. This not only limits the size of the composite to a fiber, but also consumes a lot of energy. The acoustic manipulation technique does not require a significant amount of energy, or capital equipment, nor does it produce a fiber that must be further processed to a small variety of applications. This method can effectively produce large scale composite parts in a wide variety of shapes.

The CNTs with a diameter of approximately 80 nm were aligned in planes spaced 458 μm apart by the acoustic radiation force. This forces the CNTs to aggregate together at the nodal planes. Good dispersion needs to be achieved before the alignment such that

each nanotube can bond with the matrix material. Only then can shear stresses be effectively transferred from the matrix to the filler material.

This method has been shown to be a promising method to align CNTs in a resin and three steps should be taken in the future to further demonstrate its ability: 1) shorter CNTs should be used to enhance the nanoscale alignment, 2) enhanced dispersion of CNTs should be obtained prior to alignment by BAWs using, for instance, chemical functionalization of the CNTs in combination with a tip sonicator, and 3) larger scale parts should be manufactured. Each of these steps would be helpful in establishing this alignment method among those previously demonstrated in the literature.

APPENDIX

CARBON NANOTUBE ALIGNMENT METHODS

A.1 Wet spinning

Wet spinning is accomplished by extruding a dispersed solution of a polymer and CNTs mixed in a solvent, through a spinnerette into a bath where the solvent is soluble but the polymer is not [37]. The spinnerette can have thousands of pores, making it possible to spin large quantities at once with a low spin rate [108]. The polymer precipitates out and is collected as a fiber and wound up. Wet spinning can produce CNT fibers with a high degree of alignment. Zhang et al. reported a Hermans' orientation factor $H = 0.85$ [37].

Even though spin rates achieved using this method have increased from 100 cm/min [10] to 3 m/min [68] it is still well below commercial spin rates of carbon fiber which exceed 100 m/min [109]. The method is valuable for producing fibers with aligned CNTs, but the cost limits its use to very specific and intricate applications [10]. It also only produces fibers which must be further processed for application, which is common to all spinning processes.

A.2 Melt spinning

During the melt spinning process a polymer is melted into a highly viscous liquid

state and then extruded through a spinnerette. The spinnerette typically has fewer holes than in the case of wet spinning [108]. Sometimes only a single-hole spinnerette is used to produce a thicker fiber [110]. After extrusion, the polymer is quenched with cold air to return it to a solid state. The fiber is then collected and wound up on a take-up wheel. Figure A.1 depicts the typical components used in a melt spinning process.

Potschke et al. [38] used melt spinning to align CNTs in a conductive polycarbonate composite, and achieved spin rates of up to 800 m/min, far exceeding the rates of wet spinning. They did not quantify the obtained alignment but demonstrate it through TEM images. Using one of these images an estimated orientation factor of 0.95 is found. Melt spinning is highly economical because it does not require a solvent and can yield high spin rates [108]. It does however require a heater and high pressure which amounts to a high level of input energy.

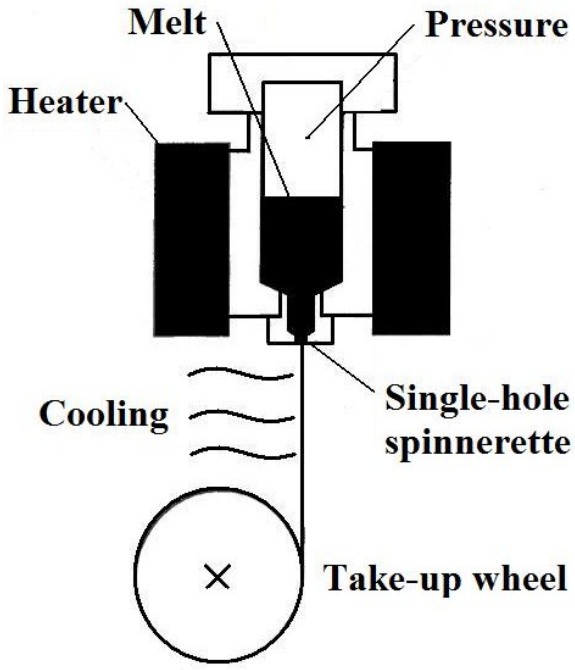

Figure A.1: Schematic of the melt spinning process [110]

A.3 Direct spinning

In the direct spinning process, CNTs are spun directly from the CVD phase [36]. High-purity CNTs are produced using CVD and then forcibly removed from the furnace by continuous wind-up. The wind-up was found to produce fibers with CNTs aligned to an average of 11° from the composite fiber direction. This equates to a Hermans' orientation factor of 0.95, an improvement to the alignment obtained by Zhang et al. using wet spinning. Li et al. also speculated that the orientation could be improved by increasing the tension on the wind-up wheel. This process is vastly different from the spinning processes discussed earlier. It requires substantial control of the chemical reactions producing the CNTs.

A.4 High strength magnetic fields

High strength magnetic fields can be used to align CNTs when applied to a dispersed mixture of CNTs. This technique is possible because CNTs display anisotropic magnetic properties [111]. It is also possible to enhance their magnetic properties with the addition of magnetic nanoparticles [112, 113]. Kimura et al. [35] aligned MWNTs in a polyester resin using a magnetic field of 10 T. The field was applied to a 1 wt% loading rate of MWNTs and good alignment was obtained. The alignment was verified with TEM images and an orientation factor of 0.92 was obtained. This method does not produce fibers like the other methods that have been discussed and allows any form part to be made as long as the magnetic field encompasses the part. The limitations to this method are the concentration of CNTs that can be used and the magnetic field strength required. Kimura et al. used only 1 wt% concentration with a 10 T magnetic field. Choi et al. [71]

performed a similar alignment at 3 wt% CNT loading rate using a 25 T magnetic field. These fields are extremely high and require special equipment. Even magnetic resonance imaging (MRI) machines do not utilize a magnetic field of this magnitude, typically being 1.5 T or 3 T [114]. Kimura et al. showed that the susceptibility of MWNTs to a magnetic field decreases with increasing concentration, making it more difficult to use a magnetic field to align the CNTs when a higher concentration is used. One reason for this is that the CNTs overlap and entangle and cannot rotate independently. Thus, for higher concentrations improved dispersion is required along with a higher magnetic field to cause effective alignment of the CNTs, two requirements that are difficult to achieve.

A.5 Mechanical stretching

Mechanically stretching a thermoplastic composite at an elevated temperature is another way to align CNTs. Jin et al. [34] performed this alignment using MWNTs in a chloroform suspension and mixed it with a thermoplastic polymer. The mixture contained 50 wt% CNTs, much higher than any loading rate previously discussed. A thin layer of this mixture was cured in a mold and then cut into strips. Each strip was stretched at a constant load and at a temperature of 100°C until the desired stretch ratio was obtained. Jin et al. reported that the composite could be stretched to 500% without fracture. Once the desired stretch ratio was obtained the sample was cooled to room temperature before releasing the load. Good alignment was obtained but was found to be significantly lower than the wet spinning alignment of Zhang. The most important advantage of this technique is that high concentrations of CNTs can be used. No other technique has exceed 10 wt% CNTs and this method is capable of handling a loading rate of 50 wt%.

The limitation of this method lies in the geometry of the parts that can be formed. Jin et al. found that thicker strips can only achieve similar alignment results if the same stretch ratio is met; however, these large stretch ratios were not able to be produced with the thicker samples. Although this thickness is not reported it is inferred to be less than the width of the samples which was 3 mm. Furthermore, the geometry of the part must be capable of being stretched in a preferential direction. This drastically limits the size and shape of the parts that can be formed with this method.

A.6 Plasma enhanced CVD

The alignment of CNTs can also be performed in conjunction with their creation. Chemical Vapor Deposition (CVD) is commonly used in the formation of CNTs and involves a gaseous source of carbon that chemically deposits on a prepared surface and the nanotubes are then grown from that surface [59]. By controlling the concentration of chemicals and the flow of gases, the diameter and length of the tubes can be controlled [115]. Bower et al. [33] demonstrated that aligned CNTs can be grown perpendicular to the surface using a plasma enhanced CVD method. The addition of a 1kW microwave plasma created an “electrical self-bias” on the substrate and allowed for the growth of the nanotubes perpendicular to the surface. Figure A.2 is an SEM image taken by Bower et al. of the aligned nanotube array. The high degree of alignment can be readily seen even at the micron level. This method has also been demonstrated without any surface preparation of the substrate, at modest temperatures, and at atmospheric pressure [23]. This could provide a means to commercially produce these aligned CNT arrays, often referred to as superaligned carbon nanotube (SACNT) arrays, at a modest cost.

This method obtains the highest degree of alignment of any method that has been previously discussed. Almost every CNT is aligned perpendicular to the substrate. The major problem of this method is how to utilize the arrays. These arrays have been used to spin yarns of aligned CNTs [116], create wafers for TEM microscopy [117], and to form an effective thin-film semi-conductor [118]. No method could be found in the literature to apply these aligned CNT arrays into a macroscale composite structure.

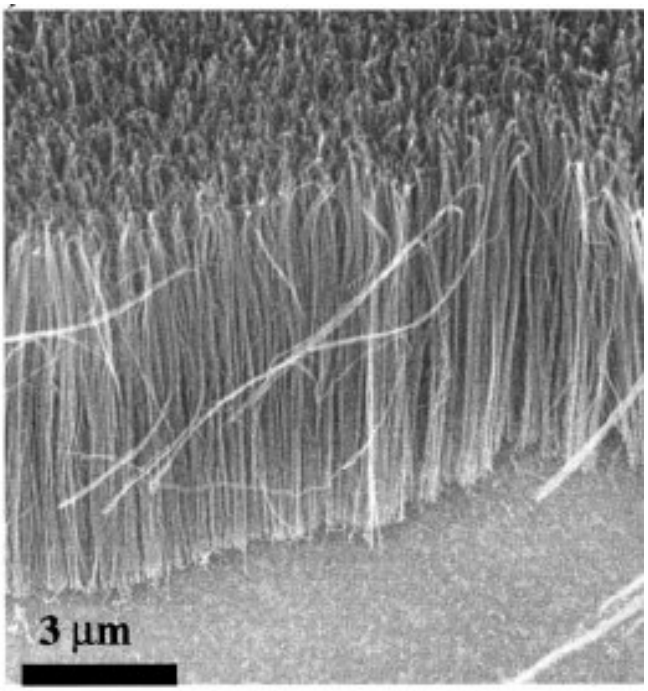

Figure A.2: SEM micrograph of an aligned array of CNTs formed by plasma enhanced CVD [33]

REFERENCES

[1] S. Iijima, "Helical microtubules of graphitic carbon," *nature,* vol. 354, pp. 56-58, 1991.

[2] R. H. Baughman, A. A. Zakhidov, and W. A. de Heer, "Carbon nanotubes--the route toward applications," *Science,* vol. 297, pp. 787-92, 2002.

[3] E. T. Thostenson, Z. Ren, and T. W. Chou, "Advances in the science and technology of carbon nanotubes and their composites: a review," *Composites science and technology,* vol. 61, pp. 1899-1912, 2001.

[4] E. T. Thostenson and T. W. Chou, "Aligned multi-walled carbon nanotube-reinforced composites: processing and mechanical characterization," *Journal of physics D: Applied physics,* vol. 35, p. L77, 2002.

[5] F. H. Gojny, M. H. G. Wichmann, U. Köpke, B. Fiedler, and K. Schulte, "Carbon nanotube-reinforced epoxy-composites: enhanced stiffness and fracture toughness at low nanotube content," *Composites science and technology,* vol. 64, pp. 2363-2371, 2004.

[6] K. Suggs and X. Q. Wang, "Structural and electronic properties of carbon nanotube-reinforced epoxy resins," *Nanoscale,* vol. 2, pp. 385-8, 2010.

[7] X. Chen, J. Wang, M. Lin, W. Zhong, T. Feng, J. Chen, and F. Xue, "Mechanical and thermal properties of epoxy nanocomposites reinforced with amino-functionalized multi-walled carbon nanotubes," *Materials Science and Engineering: A,* vol. 492, pp. 236-242, 2008.

[8] J. B. Bai, "Evidence of the reinforcement role of chemical vapour deposition multi-walled carbon nanotubes in a polymer matrix," *Carbon,* vol. 41, pp. 1325-1328, 2003.

[9] X. Xu, M. M. Thwe, C. Shearwood, and K. Liao, "Mechanical properties and interfacial characteristics of carbon-nanotube-reinforced epoxy thin films," *Applied Physics Letters,* vol. 81, p. 2833, 2002.

[10] A. B. Dalton, S. Collins, J. Razal, E. Munoz, B. G. Kim, J. N. Coleman, J. P. Ferraris, and R. H. Baughman, "Continuous carbon nanotube composite fibers: properties, potential applications, and problems," *J. Mater. Chem.,* vol. 14, pp. 1-3, 2004.

[11] J. Coleman, U. Khan, W. Blau, and Y. Gunko, "Small but strong: A review of the mechanical properties of carbon nanotube–polymer composites," *Carbon,* vol. 44, pp. 1624-1652, 2006.

[12] R. F. Gibson, *Principles of composite material mechanics*: CRC Press, 2011.

[13] G. L. Hwang, Y. T. Shieh, and K. C. Hwang, "Efficient Load Transfer to Polymer-Grafted Multiwalled Carbon Nanotubes in Polymer Composites," *Advanced Functional Materials,* vol. 14, pp. 487-491, 2004.

[14] T. Kashiwagi, J. Fagan, J. F. Douglas, K. Yamamoto, A. N. Heckert, S. D. Leigh, J. Obrzut, F. Du, S. Lin-Gibson, M. Mu, K. I. Winey, and R. Haggenmueller, "Relationship between dispersion metric and properties of PMMA/SWNT nanocomposites," *Polymer,* vol. 48, pp. 4855-4866, 2007.

[15] Y.-H. Liao, O. Marietta-Tondin, Z. Liang, C. Zhang, and B. Wang, "Investigation of the dispersion process of SWNTs/SC-15 epoxy resin nanocomposites," *Materials Science and Engineering: A,* vol. 385, pp. 175-181, 2004.

[16] C. A. Mitchell and R. Krishnamoorti, "Dispersion of Single-Walled Carbon Nanotubes in Poly (ε-caprolactone)," *Macromolecules,* vol. 40, pp. 1538-1545, 2007.

[17] C. Park, Z. Ounaies, K. A. Watson, R. E. Crooks, J. Smith, S. E. Lowther, J. W. Connell, E. J. Siochi, J. S. Harrison, and T. L. S. Clair, "Dispersion of single wall carbon nanotubes by in situ polymerization under sonication," *Chemical Physics Letters,* vol. 364, pp. 303-308, 2002.

[18] R. Rastogi, R. Kaushal, S. K. Tripathi, A. L. Sharma, I. Kaur, and L. M. Bharadwaj, "Comparative study of carbon nanotube dispersion using surfactants," *J Colloid Interface Sci,* vol. 328, pp. 421-8, 2008.

[19] J. Sandler, M. Shaffer, T. Prasse, W. Bauhofer, K. Schulte, and A. Windle, "Development of a dispersion process for carbon nanotubes in an epoxy matrix and the resulting electrical properties," *Polymer,* vol. 40, pp. 5967-5971, 1999.

[20] M. S. P. Shaffer, X. Fan, and A. Windle, "Dispersion and packing of carbon nanotubes," *Carbon,* vol. 36, pp. 1603-1612, 1998.

[21] R. Bandyopadhyaya, E. Nativ-Roth, O. Regev, and R. Yerushalmi-Rozen, "Stabilization of individual carbon nanotubes in aqueous solutions," *Nano letters,* vol. 2, pp. 25-28, 2002.

[22] P. Ajayan, O. Stephan, C. Colliex, and D. Trauth, "Aligned carbon nanotube arrays formed by cutting a polymer resin—nanotube composite," *Science,* vol. 265, pp. 1212-1214, 1994.

[23] R. Andrews, D. Jacques, A. Rao, F. Derbyshire, D. Qian, X. Fan, E. Dickey, and J. Chen, "Continuous production of aligned carbon nanotubes: a step closer to commercial realization," *Chemical Physics Letters,* vol. 303, pp. 467-474, 1999.

[24] J. Lagerwall, G. Scalia, M. Haluska, U. Dettlaff-Weglikowska, S. Roth, and F. Giesselmann, "Nanotube Alignment Using Lyotropic Liquid Crystals," *Advanced Materials,* vol. 19, pp. 359-364, 2007.

[25] J. Shaver, A. N. G. Parra-Vasquez, S. Hansel, O. Portugall, C. H. Mielke, M. Von Ortenberg, R. H. Hauge, M. Pasquali, and J. Kono, "Alignment Dynamics of Single-Walled Carbon Nanotubes in Pulsed Ultrahigh Magnetic Fields," *ACS nano,* vol. 3, pp. 131-138, 2008.

[26] C. J. Strobl, C. Schäflein, U. Beierlein, J. Ebbecke, and A. Wixforth, "Carbon nanotube alignment by surface acoustic waves," *Applied Physics Letters,* vol. 85, p. 1427, 2004.

[27] P. M. Ajayan, L. S. Schadler, C. Giannaris, and A. Rubio, "Single-walled carbon nanotube–polymer composites: strength and weakness," *Advanced Materials,* vol. 12, pp. 750-753, 2000.

[28] O. Breuer and U. Sundararaj, "Big returns from small fibers: a review of polymer/carbon nanotube composites," *Polymer composites,* vol. 25, pp. 630-645, 2004.

[29] A. K. T. Lau and D. Hui, "The revolutionary creation of new advanced materials—carbon nanotube composites," *Composites Part B: Engineering,* vol. 33, pp. 263-277, 2002.

[30] L. S. Schadler, S. C. Giannaris, and P. M. Ajayan, "Load transfer in carbon nanotube epoxy composites," *Applied Physics Letters,* vol. 73, p. 3842, 1998.

[31] V. Georgakilas, A. Bourlinos, D. Gournis, T. Tsoufis, C. Trapalis, A. Mateo-Alonso, and M. Prato, "Multipurpose organically modified carbon nanotubes: from functionalization to nanotube composites," *Journal of the American Chemical Society,* vol. 130, pp. 8733-8740, 2008.

[32] D. Roy, S. Bhattacharyya, A. Rachamim, A. Plati, and M. L. Saboungi, "Measurement of interfacial shear strength in single wall carbon nanotubes reinforced composite using Raman spectroscopy," *Journal of Applied Physics,* vol. 107, pp. 043501-043501-6, 2010.

[33] C. Bower, W. Zhu, S. Jin, and O. Zhou, "Plasma-induced alignment of carbon nanotubes," *Applied Physics Letters,* vol. 77, p. 830, 2000.

[34] L. Jin, C. Bower, and O. Zhou, "Alignment of carbon nanotubes in a polymer matrix by mechanical stretching," *Applied Physics Letters,* vol. 73, p. 1197, 1998.

[35] T. Kimura, H. Ago, M. Tobita, S. Ohshima, M. Kyotani, and M. Yumura, "Polymer composites of carbon nanotubes aligned by a magnetic field," *Advanced Materials,* vol. 14, pp. 1380-1383, 2002.

[36] Y. L. Li, I. A. Kinloch, and A. H. Windle, "Direct spinning of carbon nanotube fibers from chemical vapor deposition synthesis," *Science,* vol. 304, pp. 276-8, 2004.

[37] S. Zhang, K. K. Koziol, I. A. Kinloch, and A. H. Windle, "Macroscopic fibers of well-aligned carbon nanotubes by wet spinning," *Small,* vol. 4, pp. 1217-22, 2008.

[38] P. Pötschke, H. Brünig, A. Janke, D. Fischer, and D. Jehnichen, "Orientation of multiwalled carbon nanotubes in composites with polycarbonate by melt spinning," *Polymer,* vol. 46, pp. 10355-10363, 2005.

[39] A. Haake and J. Dual, "Micro-manipulation of small particles by node position control of an ultrasonic standing wave," *Ultrasonics,* vol. 40, pp. 317-322, 2002.

[40] W. Coakley, J. Hawkes, M. Sobanski, C. Cousins, and J. Spengler, "Analytical scale ultrasonic standing wave manipulation of cells and microparticles," *Ultrasonics,* vol. 38, pp. 638-641, 2000.

[41] S. Oberti, A. Neild, D. Möller, and J. Dual, "Towards the automation of micron-sized particle handling by use of acoustic manipulation assisted by microfluidics," *Ultrasonics,* vol. 48, pp. 529-536, 2008.

[42] A. Haake, A. Neild, D. H. Kim, J. E. Ihm, Y. Sun, J. Dual, and B. K. Ju, "Manipulation of cells using an ultrasonic pressure field," *Ultrasound in medicine & biology,* vol. 31, pp. 857-864, 2005.

[43] W. T. Coakley, D. W. Bardsley, M. A. Grundy, F. Zamani, and D. J. Clarke, "Cell manipulation in ultrasonic standing wave fields," *Journal of Chemical Technology and Biotechnology,* vol. 44, pp. 43-62, 1989.

[44] W. Coakley, G. Whitworth, M. Grundy, R. Gould, and R. Allman, "Ultrasonic manipulation of particles and cells. Ultrasonic separation of cells," *Bioseparation,* vol. 4, p. 73, 1994.

[45] B. Raeymaekers, C. Pantea, and D. N. Sinha, "Manipulation of diamond nanoparticles using bulk acoustic waves," *Journal of Applied Physics,* vol. 109, p. 014317, 2011.

[46] X. Wang, Q. Li, J. Xie, Z. Jin, J. Wang, Y. Li, K. Jiang, and S. Fan, "Fabrication of ultralong and electrically uniform single-walled carbon nanotubes on clean substrates," *Nano letters,* vol. 9, pp. 3137-3141, 2009.

[47] M. Moniruzzaman and K. I. Winey, "Polymer nanocomposites containing carbon nanotubes," *Macromolecules,* vol. 39, pp. 5194-5205, 2006.

[48] J. P. Lu, "Elastic properties of carbon nanotubes and nanoropes," *Arxiv preprint cond-mat/9704219,* 1997.

[49] W. A. De Heer, "Nanotubes and the pursuit of applications," *MRS Bulletin-Materials Research Society,* vol. 29, pp. 281-285, 2004.

[50] Q. Lu, G. Keskar, R. Ciocan, R. Rao, R. B. Mathur, A. M. Rao, and L. L. Larcom, "Determination of carbon nanotube density by gradient sedimentation," *The Journal of Physical Chemistry B,* vol. 110, pp. 24371-24376, 2006.

[51] H. Krenchel, "Fibre reinforcement," ed, 1964.

[52] H. Cox, "The elasticity and strength of paper and other fibrous materials," *British journal of applied physics,* vol. 3, p. 72, 1952.

[53] S. Hwang and R. Gibson, "Micromechanical modeling of damping in discontinuous fiber composites using a strain energy/finite element approach," *Transactions of the ASME. Journal of Engineering Materials and Technology,* vol. 109, pp. 47-52, 1987.

[54] P. Pötschke, T. Fornes, and D. Paul, "Rheological behavior of multiwalled carbon nanotube/polycarbonate composites," *Polymer,* vol. 43, pp. 3247-3255, 2002.

[55] L. Schadler and C. Galiotis, "Fundamentals and applications of micro Raman spectroscopy to strain measurements in fibre reinforced composites," *International materials reviews,* vol. 40, pp. 116-134, 1995.

[56] G. Gouadec and P. Colomban, "Raman Spectroscopy of nanomaterials: How spectra relate to disorder, particle size and mechanical properties," *Progress in Crystal Growth and Characterization of Materials,* vol. 53, pp. 1-56, 2007.

[57] L. Girifalco, M. Hodak, and R. S. Lee, "Carbon nanotubes, buckyballs, ropes, and a universal graphitic potential," *Physical Review B,* vol. 62, p. 13104, 2000.

[58] C.-H. Sun, L.-C. Yin, F. Li, G.-Q. Lu, and H.-M. Cheng, "Van der Waals interactions between two parallel infinitely long single-walled nanotubes," *Chemical Physics Letters,* vol. 403, pp. 343-346, 2005.

[59] H. Dai, "Carbon nanotubes: synthesis, integration, and properties," *Accounts of chemical research,* vol. 35, pp. 1035-1044, 2002.

[60] X. Xie, Y. Mai, and X. Zhou, "Dispersion and alignment of carbon nanotubes in polymer matrix: A review," *Materials Science and Engineering: R: Reports,* vol. 49, pp. 89-112, 2005.

[61] J. Yu, N. Grossiord, C. E. Koning, and J. Loos, "Controlling the dispersion of multi-wall carbon nanotubes in aqueous surfactant solution," *Carbon,* vol. 45, pp. 618-623, 2007.

[62] D. Wang, W. X. Ji, Z. C. Li, and L. Chen, "A biomimetic “polysoap” for single-walled carbon nanotube dispersion," *Journal of the American Chemical Society,* vol. 128, pp. 6556-6557, 2006.

[63] J. Vera-Agullo, A. Glória-Pereira, H. Varela-Rizo, J. L. Gonzalez, and I. Martin-Gullon, "Comparative study of the dispersion and functional properties of multiwall carbon nanotubes and helical-ribbon carbon nanofibers in polyester nanocomposites," *Composites science and technology,* vol. 69, pp. 1521-1532, 2009.

[64] Z. Jin, K. Pramoda, G. Xu, and S. H. Goh, "Dynamic mechanical behavior of melt-processed multi-walled carbon nanotube/poly (methyl methacrylate) composites," *Chemical Physics Letters,* vol. 337, pp. 43-47, 2001.

[65] P. Pötschke, A. R. Bhattacharyya, and A. Janke, "Melt mixing of polycarbonate with multiwalled carbon nanotubes: microscopic studies on the state of dispersion," *European Polymer Journal,* vol. 40, pp. 137-148, 2004.

[66] Z. Liang, J. Gou, C. Zhang, B. Wang, and L. Kramer, "Investigation of molecular interactions between (10, 10) single-walled nanotube and Epon 862 resin/DETDA curing agent molecules," *Materials Science and Engineering: A,* vol. 365, pp. 228-234, 2004.

[67] H. D. Wagner, O. Lourie, Y. Feldman, and R. Tenne, "Stress-induced fragmentation of multiwall carbon nanotubes in a polymer matrix," *Applied Physics Letters,* vol. 72, p. 188, 1998.

[68] V. Mottaghitalab, G. M. Spinks, and G. G. Wallace, "The influence of carbon nanotubes on mechanical and electrical properties of polyaniline fibers," *Synthetic Metals,* vol. 152, pp. 77-80, 2005.

[69] R. Haggenmueller, H. Gommans, A. Rinzler, J. E. Fischer, and K. Winey, "Aligned single-wall carbon nanotubes in composites by melt processing methods," *Chemical Physics Letters,* vol. 330, pp. 219-225, 2000.

[70] J. Gao, M. E. Itkis, A. Yu, E. Bekyarova, B. Zhao, and R. C. Haddon, "Continuous spinning of a single-walled carbon nanotube-nylon composite fiber," *Journal of the American Chemical Society,* vol. 127, pp. 3847-3854, 2005.

[71] E. S. Choi, J. S. Brooks, D. L. Eaton, M. S. Al-Haik, M. Y. Hussaini, H. Garmestani, D. Li, and K. Dahmen, "Enhancement of thermal and electrical properties of carbon nanotube polymer composites by magnetic field processing," *Journal of Applied Physics,* vol. 94, p. 6034, 2003.

[72] M. Fujiwara, E. Oki, M. Hamada, Y. Tanimoto, I. Mukouda, and Y. Shimomura, "Magnetic orientation and magnetic properties of a single carbon nanotube," *The Journal of physical chemistry A,* vol. 105, pp. 4383-4386, 2001.

[73] Z. Fan and S. G. Advani, "Characterization of orientation state of carbon nanotubes in shear flow," *Polymer,* vol. 46, pp. 5232-5240, 2005.

[74] Z. Huang, J. Xu, Z. Ren, J. Wang, M. Siegal, and P. Provencio, "Growth of highly oriented carbon nanotubes by plasma-enhanced hot filament chemical vapor deposition," *Applied Physics Letters,* vol. 73, pp. 3845-3847, 1998.

[75] T. Kozuka, T. Tuziuti, H. Mitome, and T. Fukuda, "Acoustic manipulation of micro objects using an ultrasonic standing wave," 1994, p. 83.

[76] M. Barmatz and P. Collas, "Acoustic radiation potential on a sphere in plane, cylindrical, and spherical standing wave fields," *The Journal of the Acoustical Society of America,* vol. 77, p. 928, 1985.

[77] T. Hasegawa, "Acoustic radiation force on a sphere in a quasistationary wave field—theory," *The Journal of the Acoustical Society of America,* vol. 65, p. 32, 1979.

[78] T. Hasegawa and K. Yosioka, "Acoustic-Radiation Force on a Solid Elastic Sphere," *The Journal of the Acoustical Society of America,* vol. 46, p. 1139, 1969.

[79] L. V. King, "On the acoustic radiation pressure on spheres," *Proceedings of the Royal Society of London. Series A-Mathematical and Physical Sciences,* vol. 147, pp. 212-240, 1934.

[80] W. L. Nyborg, "Radiation pressure on a small rigid sphere," *Journal of the Acoustical Society of America,* vol. 42, pp. 947-952, 1967.

[81] K. Yosioka and Y. Kawasima, "Acoustic radiation pressure on a compressible sphere," *Acustica,* vol. 5167, 1955.

[82] L. Gor'Kov, "On the forces acting on a small particle in an acoustical field in an ideal fluid," 1962, p. 773.

[83] J. Awatani, "Study on acoustic radiation pressure (IV), radiation pressure on a cylinder," *Mem. Inst. Sci. Osaka University,* vol. 12, pp. 95-102, 1955.

[84] T. Hasegawa, K. Saka, N. Inoue, and K. Matsuzawa, "Acoustic radiation force experienced by a solid cylinder in a plane progressive sound field," *The Journal of the Acoustical Society of America,* vol. 83, p. 1770, 1988.

[85] D. Haydock, "Calculation of the radiation force on a cylinder in a standing wave acoustic field," *Journal of Physics A: Mathematical and General,* vol. 38, pp. 3279-3285, 2005.

[86] F. G. Mitri, "Theoretical calculation of the acoustic radiation force acting on elastic and viscoelastic cylinders placed in a plane standing or quasistanding wave field," *The European Physical Journal B,* vol. 44, pp. 71-78, 2005.

[87] W. Wei, D. B. Thiessen, and P. L. Marston, "Acoustic radiation force on a compressible cylinder in a standing wave," *The Journal of the Acoustical Society of America,* vol. 116, p. 201, 2004.

[88] J. Wu, G. Du, S. S. Work, and D. M. Warshaw, "Acoustic radiation pressure on a rigid cylinder: An analytical theory and experiments," *The Journal of the Acoustical Society of America,* vol. 87, pp. 581-586, 1990.

[89] F. F. Abraham, "Functional Dependence of Drag Coefficient of a Sphere on Reynolds Number," *Physics of Fluids,* vol. 13, p. 2194, 1970.

[90] P. P. Brown and D. F. Lawler, "Sphere drag and settling velocity revisited," *Journal of Environmental Engineering,* vol. 129, p. 222, 2003.

[91] B. Cichocki and K. Hinsen, "Stokes drag on conglomerates of spheres," *Physics of Fluids,* vol. 7, p. 285, 1995.

[92] P. S. Granville, "The calculation of the viscous drag of bodies of revolution," DTIC Document1953.

[93] B. Huner and R. G. Hussey, "Cylinder drag at low Reynolds number," *Physics of Fluids,* vol. 20, p. 1211, 1977.

[94] M. Dorrestijn, A. Bietsch, T. Açıkalın, A. Raman, M. Hegner, E. Meyer, and C. Gerber, "Chladni Figures Revisited Based on Nanomechanics," *Physical Review Letters,* vol. 98, 2007.

[95] F. Du Toit, R. Sanderson, W. Engelbrecht, and J. Wagener, "The effect of surface fluorination on the wettability of high density polyethylene," *Journal of fluorine chemistry,* vol. 74, pp. 43-48, 1995.

[96] P. Ceramics, "Principles and Applications," ed: APC International Ltd, 2006.

[97] J. Gallego-Juarez, "Piezoelectric ceramics and ultrasonic transducers," *Journal of Physics E: Scientific Instruments,* vol. 22, p. 804, 1989.

[98] K. Uchino, "Introduction to Piezoelectric Actuators and Transducers," DTIC Document2003.

[99] M. Viana, P. Jouannin, C. Pontier, and D. Chulia, "About pycnometric density measurements," *Talanta,* vol. 57, pp. 583-593, 2002.

[100] B. V. Antohe and D. B. Wallace, "The determination of the speed of sound in liquids using acoustic resonance in piezoelectric tubes," *Measurement Science and Technology,* vol. 10, p. 994, 1999.

[101] J. Hermans, P. Hermans, D. Vermaas, and A. Weidinger, "Quantitative evaluation of orientation in cellulose fibres from the X-ray fibre diagram," *Recueil des Travaux Chimiques des Pays-Bas,* vol. 65, pp. 427-447, 1946.

[102] A. R. Bhattacharyya, T. Sreekumar, T. Liu, S. Kumar, L. M. Ericson, R. H. Hauge, and R. E. Smalley, "Crystallization and orientation studies in polypropylene/single wall carbon nanotube composite," *Polymer,* vol. 44, pp. 2373-2377, 2003.

[103] T. V. Sreekumar, T. Liu, B. G. Min, H. Guo, S. Kumar, R. H. Hauge, and R. E. Smalley, "Polyacrylonitrile single-walled carbon nanotube composite fibers," *Advanced Materials,* vol. 16, pp. 58-61, 2004.

[104] H. Koerner, G. Price, N. A. Pearce, M. Alexander, and R. A. Vaia, "Remotely actuated polymer nanocomposites—stress-recovery of carbon-nanotube-filled thermoplastic elastomers," *Nature Materials,* vol. 3, pp. 115-120, 2004.

[105] B. Krause, P. Pötschke, and L. Häußler, "Influence of small scale melt mixing conditions on electrical resistivity of carbon nanotube-polyamide composites," *Composites science and technology,* vol. 69, pp. 1505-1515, 2009.

[106] D. O'Regan and B. Meenan, "A comparison of Young's modulus predictions in fibre-reinforced-polyamide injection mouldings," *Composites science and technology,* vol. 59, pp. 419-427, 1999.

[107] K. Schulte, F. H. Gojny, B. Fiedler, J. K. W. Sandler, and W. Bauhofer, "Carbon Nanotube-Reinforced Polymers: a State of the Art Review," *Polymer composites,* pp. 3-23, 2005.

[108] "man-made fibre," in *Encyclopaedia Brittanica*, Online Edition ed: Encyclopaedia Brittanica Inc., 2012.

[109] G. Capone, "Wet-spinning technology," *Acrylic Fiber Technology and Applications,* pp. 69-103, 1995.

[110] R. Andrews, D. Jacques, A. M. Rao, T. Rantell, F. Derbyshire, Y. Chen, J. Chen, and R. C. Haddon, "Nanotube composite carbon fibers," *Applied Physics Letters,* vol. 75, p. 1329, 1999.

[111] J. Lu, "Novel Magnetic Properties of Carbon Nanotubes," *Physical Review Letters,* vol. 74, pp. 1123-1126, 1995.

[112] M. A. Correa-Duarte, M. Grzelczak, V. Salgueiriño-Maceira, M. Giersig, L. M. Liz-Marzán, M. Farle, K. Sierazdki, and R. Diaz, "Alignment of carbon nanotubes under low magnetic fields through attachment of magnetic nanoparticles," *The Journal of Physical Chemistry B,* vol. 109, pp. 19060-19063, 2005.

[113] G. Korneva, H. Ye, Y. Gogotsi, D. Halverson, G. Friedman, J. C. Bradley, and K. G. Kornev, "Carbon nanotubes loaded with magnetic particles," *Nano letters,* vol. 5, pp. 879-884, 2005.

[114] V. L. Yarnykh, M. Terashima, C. E. Hayes, A. Shimakawa, N. Takaya, P. K. Nguyen, J. H. Brittain, M. V. McConnell, and C. Yuan, "Multicontrast black-blood MRI of carotid arteries: Comparison between 1.5 and 3 tesla magnetic field strengths," *Journal of Magnetic Resonance Imaging,* vol. 23, pp. 691-698, 2006.

[115] Y. C. Choi, Y. M. Shin, Y. H. Lee, B. S. Lee, G. S. Park, W. B. Choi, N. S. Lee, and J. M. Kim, "Controlling the diameter, growth rate, and density of vertically aligned carbon nanotubes synthesized by microwave plasma-enhanced chemical vapor deposition," *Applied Physics Letters,* vol. 76, p. 2367, 2000.

[116] X. Zhang, K. Jiang, C. Feng, P. Liu, L. Zhang, J. Kong, T. Zhang, Q. Li, and S. Fan, "Spinning and Processing Continuous Yarns from 4-Inch Wafer Scale Super-Aligned Carbon Nanotube Arrays," *Advanced Materials,* vol. 18, pp. 1505-1510, 2006.

[117] L. Zhang, C. Feng, Z. Chen, L. Liu, K. Jiang, Q. Li, and S. Fan, "Superaligned Carbon Nanotube Grid for High Resolution Transmission Electron Microscopy of Nanomaterials," *Nano letters,* vol. 8, pp. 2564-2569, 2008.

[118] S. J. Kang, C. Kocabas, T. Ozel, M. Shim, N. Pimparkar, M. A. Alam, S. V. Rotkin, and J. A. Rogers, "High-performance electronics using dense, perfectly aligned arrays of single-walled carbon nanotubes," *Nature Nanotechnology,* vol. 2, pp. 230-236, 2007.